CHAPTER 4: Ni doped Ag_2O photocatalysts

4.1 Introduction

Defects such as doping and vacancies change photocatalysts' electronic structure and adsorption properties. These can widen or narrow the bandgap of the native material (C. Feng et al., 2020; Kamarulzaman et al., 2015; Junpeng Wang et al., 2012; X. Yan et al., 2017; X. Zhou et al., 2011; D. Zhu & Zhou, 2021). For example, the white color of anatase TiO_2 can change into blue or red due to different defects and could worsen or improve its adsorption properties towards a molecule (Maarisetty & Baral, 2020). For instance, density functional theory (DFT) calculations have pointed out that Ga and N vacancies on the GaN surface could change adsorption behavior (Ji et al., 2014). In another case, oxygen vacancies (OV) in ceria (CeO_2) altered its bandgap and demonstrated enhanced CO_2 reduction photocatalytic efficiency (Hezam et al., 2020). Doping or vacancies also improve the charge separation in a photocatalyst after its photo-excitation (Jin et al., 2021; Shan et al., 2017; B. Zhang et al., 2017; D. Zhang et al., 2020, 2021; K. Zhao et al., 2020). OV can also act as oxygen adsorption sites, increasing the percentage of chemisorbed oxygen on the photocatalyst surface. Photo-excited electrons can reduce chemisorbed oxygen to give active species like superoxide radicals (M. Li et al., 2021).

There are only a few investigations that have included both oxygen vacancies and dopants in one-phase photocatalysts. Thus, Tang et al. analyzed the electronic structure of Cd_2SnO_4 having oxygen vacancies along with La doping through DFT calculations. The two types of defects in Cd_2SnO_4 increased the bandgap and led to an overlap of the Fermi level with the conduction band (Tang et al., 2018b). Recently, Pan et al. found that doping hematite with Sn or Ti was favorable for oxygen vacancy generation and improved its photocatalytic properties (Pan et al., 2020). It seemed that the accumulation of donor levels in the bandgap of hematite diminished it. Recently, Ahmed et al. substituted Sn^{4+} with Sr^{2+} in SnO_2. The substitution by lower oxidation state Sr^{2+} provoked oxygen vacancies in the SnO_2 lattice for maintaining charge neutrality (Ahmed et al., 2019). Nevertheless, there is a lack of research on the effect of a combination of oxygen vacancies and doping on photocatalyst properties.

There is a preference for moderate band gap photocatalysts because they can utilize more spectrum of solar radiation (Jun Chen et al., 2016; Rawal et al., 2013). In this respect, Ag_2O is an exciting candidate. Being a relatively small bandgap (1.2 – 1.4 eV) semiconductor, it gets photo-excited by most light under the UV-visible range in the solar spectrum. But, nanoparticles of Ag_2O have poor photo-stability. A frequent observation is the conversion of Ag^+ into Ag during the use of Ag_2O as a photocatalyst (Xuefei Wang et al., 2011). Proper charge separation can solve or significantly reduce this problem (L. Pei et al., 2019, 2020). Hence, a few reports have demonstrated the construction of efficient heterojunction photocatalysts with Ag_2O as one of the components (Yuqi Cui et al., 2017a; S. Kumar et al., 2018b; Pal et al., 2020; P.-Q. Wang et al., 2013).

Furthermore, doping can also improve charge separation in photocatalysts. Thus, De et al. showed that Zn doped Ag_2O had demonstrated improved charge separation and better photocatalytic activity for methyl orange degradation. Zn doping also widened the Ag_2O bandgap to 1.64 eV (De et al., 2020). Another latest study showed that the doping of Ag_2O by Sr could increase its bandgap and photocatalysis efficiency (Kiani et al., 2019). A few publications have also used DFT calculations to investigate the effect of oxygen vacancies on the electronic structure of Ag_2O (Allen et al., 2011; Tezsevin et al., 2018; Yin et al., 2016). For instance, DFT calculations by Ribeiro et al. disclosed Ag-O bond elongation near the oxygen vacancy site. Consequently, the conduction band (CB) and valence band (VB) positions got affected and widened the material's bandgap (Ribeiro et al., 2020). But, an extensive literature survey shows no experimental studies on the photocatalytic properties of Ag_2O nanoparticles with oxygen vacancies.

Given the above discussion, the first objective of the present study was to prepare Ag_2O nanoparticles with oxygen vacancies using a hydrothermal protocol. The high pressure generated during hydrothermal synthesis stabilized the sample's structural strains induced by oxygen vacancies (Ding et al., 2020; Z. Li et al., 2019). Next, we prepared Ni-doped Ag_2O nanoparticles. Because Ni is in a +2 oxidation state, doping injects excess electrons into the Ag_2O lattice. The latter can increase the extent of chemisorbed oxygens on the photocatalyst surface. Doping Ag_2O by Ni can also influence the adsorption properties of the prepared nanomaterial. Previously published literature suggests that NiO is an efficient adsorbent of ciprofloxacin (CIP) antibiotics which is a significant risk for the environment (Girardi et al., 2011; Hu et al., 2019; Jia et al., 2020). Because of this, it was thought that Ni-doping of Ag_2O nanoparticles could improve their adsorption and CIP photocatalytic degradation properties. Excepting the addition of the Ni salt, the preparation protocol of Ni-doped Ag_2O nanoparticles remained the same.

Plane-wave DFT calculations and X-ray diffraction (XRD) analysis have been employed to analyze the vital question of whether the dopant (Ni^{2+}) will substitute Ag^+ in Ag_2O or occupy an interstitial site. DFT calculations also gave qualitative insight into the changes in electronic structure induced by an oxygen vacancy and the dopant. XPS study demonstrated the quantitative analysis of oxygen vacancy. The photocatalytic activities of doped and undoped Ag_2O nanoparticle samples were evaluated for CIP degradation. Photoluminescence studies revealed the effect of doping on photoexcited electron-hole recombination. Experiments were also carried out in the presence of suitable scavenger molecules specific to different active species like hydroxyl, superoxide radicals, and holes.

4.2 Experimental Section

4.2.1 Sample preparation

For the hydrothermal synthesis of Ag_2O nanoparticles, 2 mmol of $AgNO_3$ was dissolved in a 50 ml volume of deionized double distilled water (DDDW) along with continuous stirring for 15 minutes. Next, the pH of the solution was increased to 11 by dropwise addition of 0.2M NaOH. At this stage, the formation of a brown-colored precipitate was observed. The whole reaction mixture was shifted to a 100 ml stainless steel autoclave and subjected to heat treatment at 180^0C for 24 hours in an oven. A black solid material obtained at the end of the process was separated and washed with DDDW repeatedly until the water used for washing had a neutral pH. The solid product was dried in a hot air oven at 50^0C, and N0 hereafter denotes this Ag_2O nanoparticle powder sample in the rest of this chapter.

For Ni-doped Ag_2O preparation, just like earlier, an aqueous solution of $AgNO_3$ was prepared in DDDW along with continuous stirring for 15 minutes. Then the pH of the $AgNO_3$ solution was increased to 11 by dropwise addition of 0.2M NaOH. At this stage, the desired amount of Ni salt (aqueous solution form) was added dropwise to the previously obtained brown-colored reaction mixture. The overall mixture was stirred for another 15 minutes, maintaining the pH of the solution at 11. Next, this reaction mixture was transferred into a 100 ml stainless steel autoclave and kept in an oven at 180^0C for 24 hours. The as-obtained solid product was washed and dried at 50^0C to get the Ni-doped Ag_2O nanoparticles (N1, N2, N3) samples. Three Ni-doped Ag_2O nanoparticle samples with different Ni percentages were prepared. Samples N1, N2, and N3 represent 1.25, 2.5, and 5-mole percent of $Ni(NO_3)_2.6H_2O$ salt in the Ni-doped Ag_2O preparation.

4.2.2 DFT calculations

All plane-wave density functional theory (DFT) calculations were done using the Vienna ab-initio simulation package (VASP 5.4.4) on the MedeA molecular modeling software interface (version 1.0). The defect formation energy and other calculations used the generalized gradient approximation (GGA) Perdew-Burke-Ernzerhoff (PBE) exchange-correlation functional with Projected Augmented Wave (PAW) pseudopotentials. The initial step was constructing a 2x2x2 supercell of the Ag_2O unit cell (Card No: COD 4318188). The k-points and basis set cut-off parameters were varied for this supercell, and the parameters with minimum energies were used for further calculations. Full structure optimization was carried out at 4x4x4 k-point mesh size and plane-wave basis set cut-off value of 400 eV. Next, structure optimization was carried out for Ag_2O supercells with a Ni atom substituting an Ag atom, and in another doping case, the Ni atom occupied an interstitial position. The defect formation energy for substitutionally and interstitially doped Ag_2O systems were computed using equations (4.1) and (4.2).

$$E_f = E_{defect}(D1) - [E_{perfect}(Ag_2O) - \mu_{Ag} + \mu_{Ni}] \tag{4.1}$$

$$E_f = E_{defect}(D2) - [E_{perfect}(Ag_2O) + \mu_{Ni}] \tag{4.2}$$

Here E_f is the defect formation energy, $E_{defect}(D1)$ the energy of the D1 (substitutional doping), $E_{defect}(D2)$ (interstitially doped) the energy of the D2, μ_{Ni} and μ_{Ag} are the chemical potentials of Ni and Ag. Equation (1) gives the formation energy for the model with the substitutional defect (D1), while equation (2) was utilized to calculate the same for the interstitial defect system (D2). The OV-mediated Ag_2O model was constructed by deleting one oxygen from the Ag_2O supercell. DFT computations were also implemented on an Ag_2O supercell with an oxygen vacancy and an Ag substituted by a Ni atom. Then, we collected spin-polarized DOS for both cases under $8 \times 8 \times 8$ k-points and 400eV cut-off calculation parameters.

4.2.3 Photocatalytic activity measurements

The photocatalytic activities of the Ag_2O samples with oxygen vacancies and Ni-doping were assessed for CIP degradation. Exactly 3 ml of (4.5 ppm) CIP aqueous solution and 0.1 mg photocatalyst were mixed together in a 4 ml quartz cuvette with 1 cm of path length. The overall pH of this mixture was maintained at three by the addition of 0.1M HCl. The mixture was stirred for 1 hour in a dark environment to ensure the complete adsorption-desorption equilibrium. Then, the mixture was placed in a homemade photocatalytic chamber for visible light irradiation. The visible light source was a 14W Philips cool LED bulb. The UV-visible absorption spectrum of the reaction mixture was recorded every 5 minutes time interval. Turnover frequencies (TOF) were calculated to quantify the photocatalytic efficiencies of the Ag_2O samples prepared in this study.

4.3 Result and discussion

4.3.1 Structural Properties:

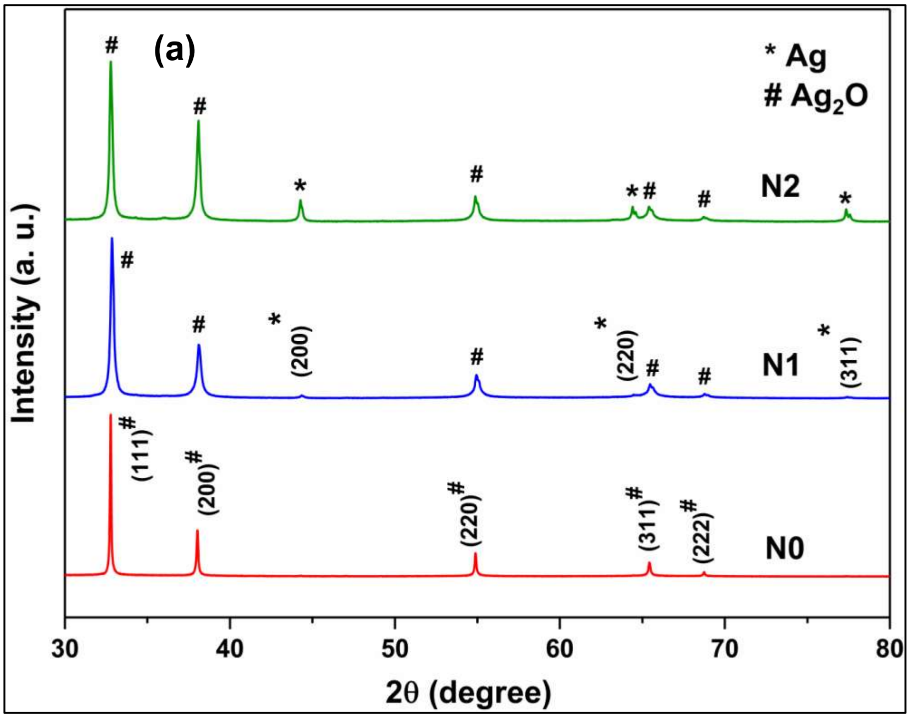

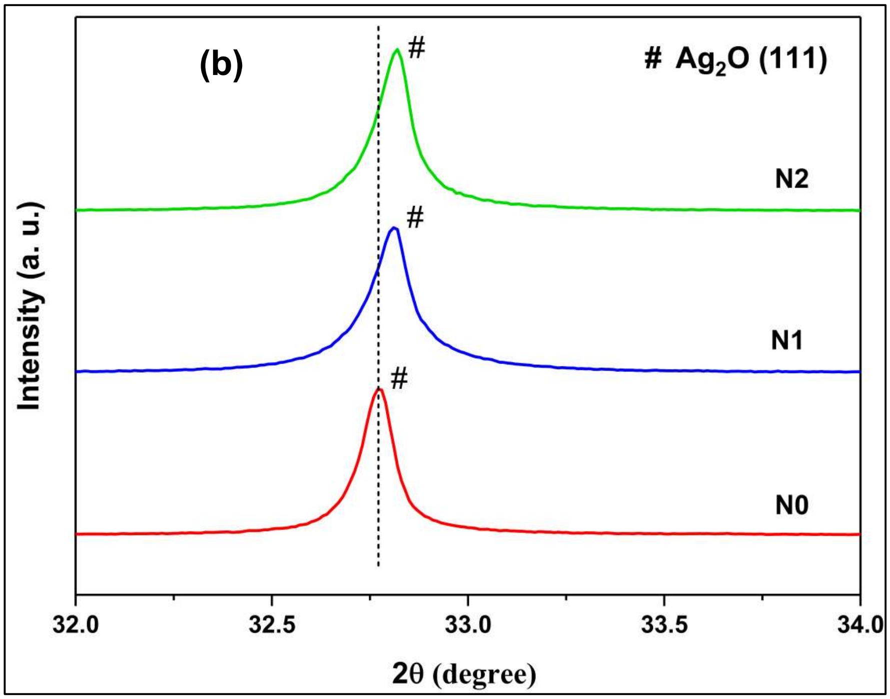

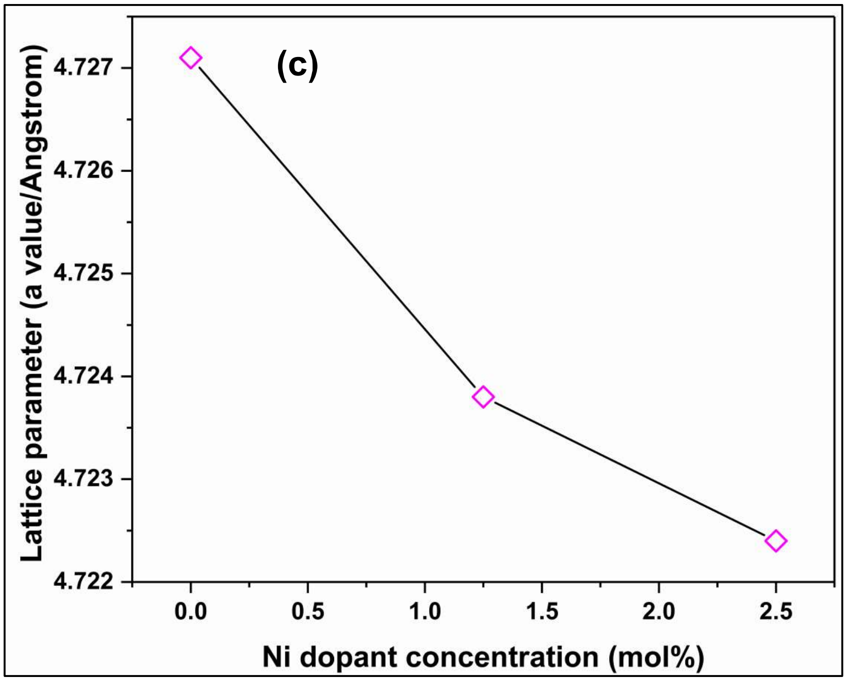

Figure 4.1 (a) The X-ray diffraction patterns of N0, N1, and N2 samples, (b) The HR-XRDs of the region around the Ag_2O (111) peak for N0, N1, and N2 samples, (c) Lattice parameter change with dopant concentration.

Figure 4.1a shows the powder XRD pattern of doped (N1 & N2) and undoped (N0) nanoparticle samples. All peaks in the XRD of the N0 sample could be indexed to the FCC Ag_2O phase. There was no formation of any other phase in this sample. The peaks in the XRDs of the doped samples (N1 and N2) match with those of the standard FCC Ag_2O (JCPDS Card No. 75-1532) phase and also metallic FCC Ag phase (JCPDS Card No. 89-3722). There are no NiO phase peaks in the XRD patterns of either N1 or N2 samples. On increasing the dopant concentration to 5 mol% in the N3 sample, there is NiO phase formation.

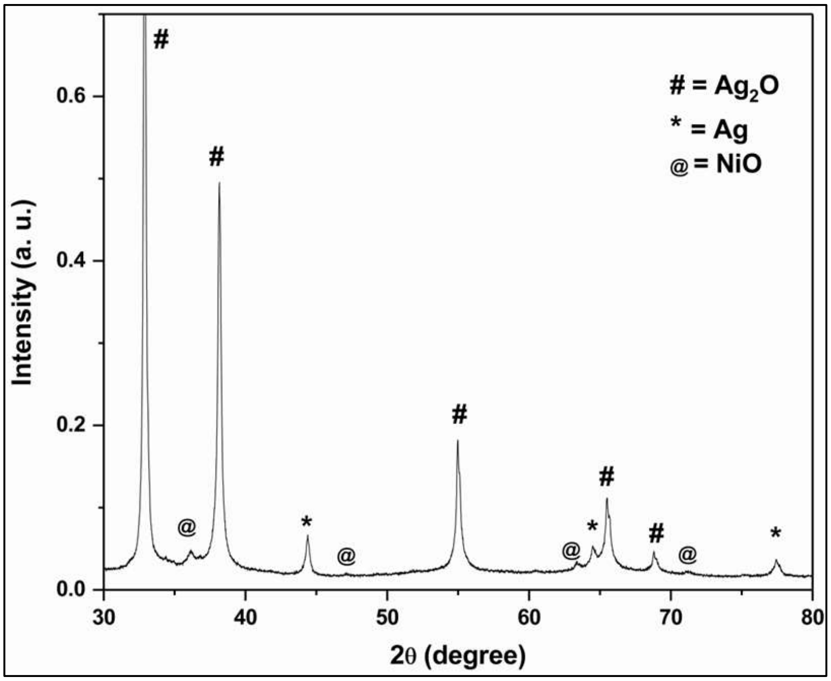

Figure 4.2 Powder XRD patterns of N3 sample.

Figure 4.2 shows the powder XRD pattern of the N3 sample. The peaks at 2θ values 36.2, 37, 62.87, and 75.20 correspond to NiO in the N3 sample (Wei et al., 2009). Given the formation of a separate NiO phase in the N3 doped Ag_2O sample and no formation of a Ni-Ag_2O solid solution, we do not characterize or evaluate the photocatalytic activity of this sample any further in this study.

Figure 4.1b displays the HR-XRD patterns of N0, N1, and N2 samples. It shows that the Ag_2O (111) peak shifts towards a higher 2θ or smaller d-values with an increase in dopant concentration (up to 2.5-mole percent). Figure 4.1c gives the change in lattice parameters with dopant concentration. Here, the plot deviates slightly from the linear relationship. The deviation from the linearity or Vegard's law is caused by size mismatch between the dopant and the Ag^+ in Ag_2O. There is a decrease in lattice parameter with Ni-dopant concentration. Thus, the Ag_2O lattice contracts with dopant concentration. The effective ionic radii values of Ni^{2+} and Ag^+ are 69 and 115 pm, respectively. The dopant Ni atom can either occupy an interstitial site or substitute an Ag atom in the Ag_2O lattice. Lattice contraction will happen if the smaller Ni replaces the Ag in the Ag_2O structure. The occupation of a smaller interstitial void by the relatively larger Ni would have expanded the Ag_2O lattice. Since the lattice has contracted, the HR-XRD patterns' analysis points to the substitution of Ag by Ni in the Ag_2O lattice.

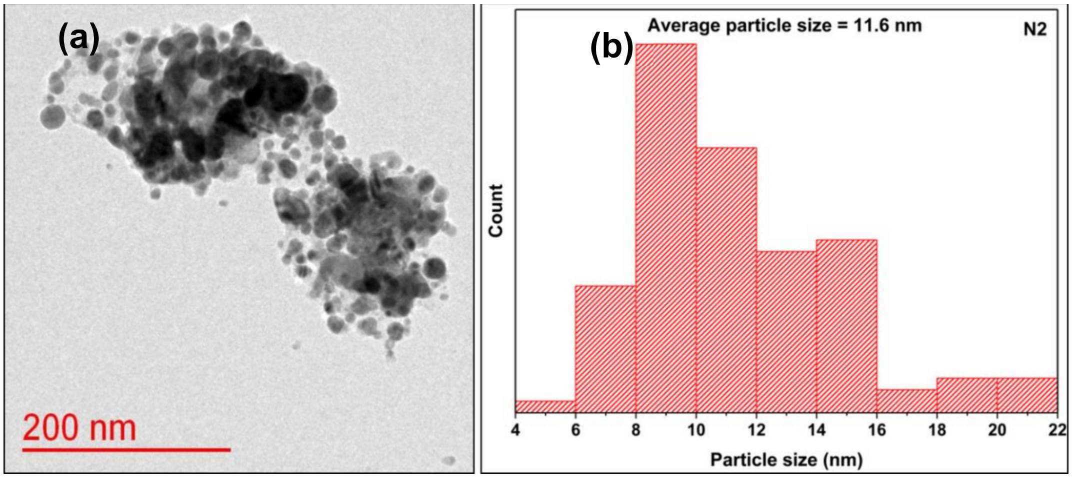

Figure 4.3 (a) A TEM image and (b) particle size distribution curve of N2 sample.

The morphologies of Ni-doped Ag_2O nanoparticles were analyzed from their TEM micrographs. Figure 4.3 displays a typical TEM image of the N2 nanoparticles and the sample's particle size distribution. Figure 4.4 shows a TEM micrograph of sample N0.

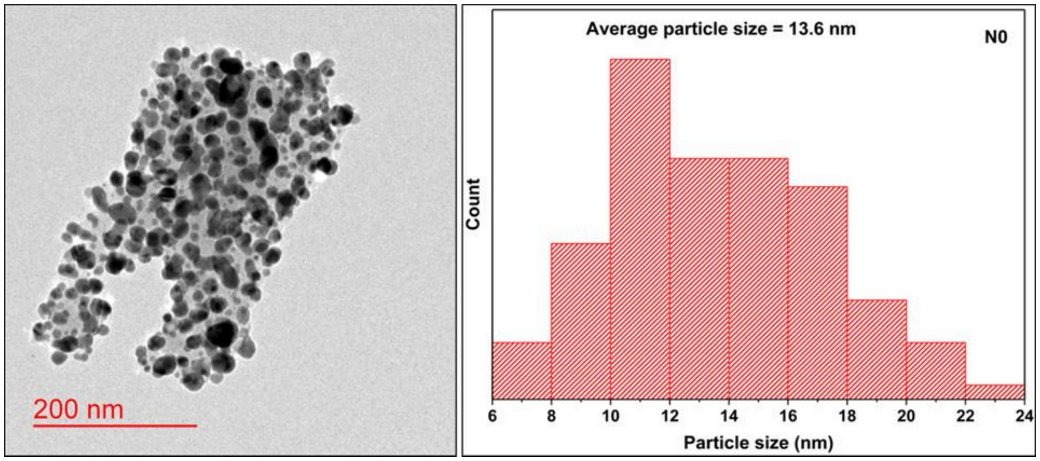

Figure 4.4 A TEM micrograph and particle size distribution of N0 sample.

The nanoparticles are approximately spherical in both samples. The average particle size of the nanoparticles in the N2 sample is ~ 11.6 nm. In contrast, the average particle size of sample N0 is ~13.6 nm. The decrease in the particle size compared to the pure one is a natural phenomenon of doping. The different size and charge of the dopant atoms disrupt the regular crystal lattice making up pure Ag_2O particles, resulting in smaller nanoparticle sizes (G. Xiang et al., 2015). Figure 4.5 shows the EDS data of the N2 sample, demonstrating the presence of Ni in the doped sample.

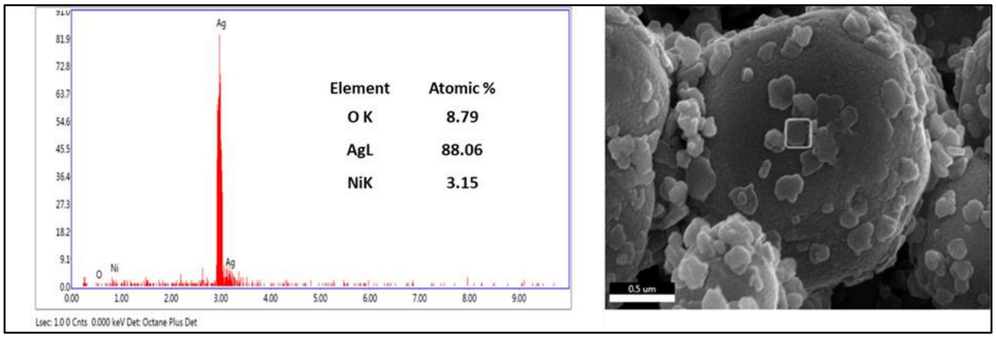

Element	Atomic %
O K	8.79
AgL	88.06
NiK	3.15

Figure 4.5 The EDS spectrum and a SEM image of N2.

4.3.2 XPS analysis

Analyzing the XPS survey spectra of N0, N1, and N2 (Figure 4.6) enabled identifying the elements present in these samples. Table 4.1 lists the atomic percent of all the elements present in N0, N1, and N2 samples. It is observed that Ni doping percentage increases from N1 to N2. Atomic percentages of Ag and O in sample N0 are 68.68 and 31.32, respectively. Sample N2 has 2.28% Ni, 59.27% Ag, and 38.45% O. We deconvolute and analyze the high-resolution O1s and Ag 3d peaks to determine various oxidation and defect states.

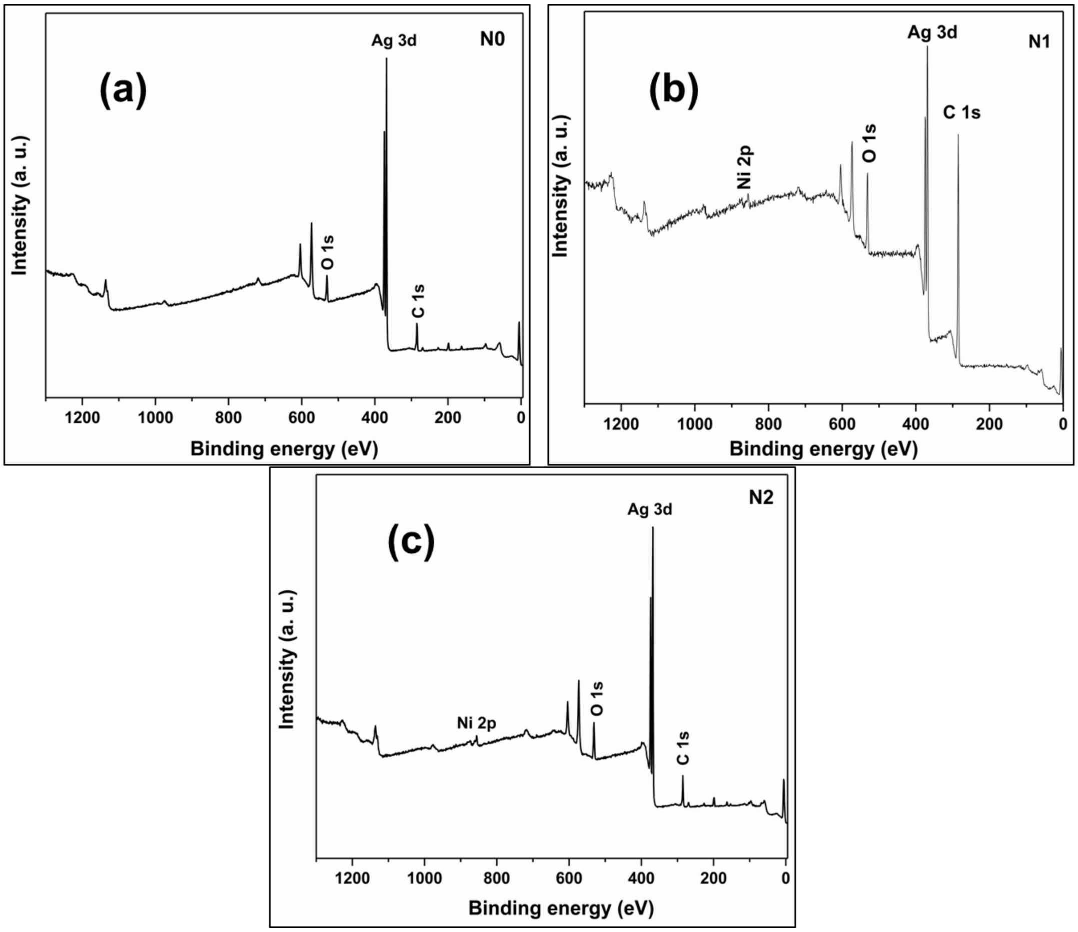

Figure 4.6 XPS survey spectrum of (a) N0, (b) N1, and (c) N2 samples.

Table 4.1 Elemental analysis of the N0, N1, and N2 samples using XPS.

S. No.	Sample name	% Atomic concentration of elements		
		Ag 3d	O 1s	Ni 2p
1	N0	68.68	31.32	-
2	N1	45.78	52.51	1.71
3	N2	59.27	38.45	2.28

The high-resolution O1s region in the XPS of N0 and N2 gave a quantitative description of the oxygen defects in the undoped and doped samples. The deconvoluted O1s peaks of both N0 and N2 show that they are composed of lattice oxygen (O_L), vacancy oxygen (O_V), and chemisorbed oxygen (O_C). Note that O_V defects can be analyzed by such deconvolution of the XPS O1s peak in literature (Ding et al., 2020; Junpeng Wang et al., 2012; Q. Zhang et al., 2020). Figure 4.8a shows that the relative percentages of the O_L, $O_{V,}$ and O_C species are 14.62, 56.54, and 28.84 %, respectively, for the N0 sample. In contrast, the relative percentages of these oxygen species in the N2 sample are 10.39% O_L, 40.98% $O_{V,}$ and 48.62 % O_C (Figure 4.8b). This result indicates Ni doping increased chemisorbed oxygen but decreased oxygen vacancies relative to N0. As mentioned earlier, the high autogenous pressure built up during hydrothermal synthesis can induce oxygen vacancies in the sample. Therefore, the undoped sample also possesses OVs. Doping also decreased the binding energy of the chemisorbed oxygen from 532.41 eV (N0) to 532 eV (N2). The O_C binding energy decrease after doping points to the transfer of the electron density to the chemisorbed oxygen in N2. Higher electron density on the chemisorbed oxygen seems to be more effective in activating superoxide radical formation during the photocatalytic process (N. Zhang et al., 2016).

The crystal structure of Ag_2O with oxygen vacancy defects displays two types of oxygen binding energy signals. One peak is due to O_L, having perfect Ag-O coordination. The second peak is due to O_V or oxygens (adjacent to the vacancy in the anion sub-lattice) having defect coordination different from the perfect Ag-O coordination number (Gao et al., 2017). Hence, the O_V percentage is a number proportional to the oxygen vacancies. Notably, surface-bound chemisorbed oxygen (O_C) is not a part of the Ag_2O lattice. Therefore, the oxygen in the Ag_2O lattice (N0) is 71.16% (O_L+O_V) of the total oxygen making up the O1s peak. A similar calculation reveals that O_L+O_V for N2 is 51.37% of the total oxygen in the sample.

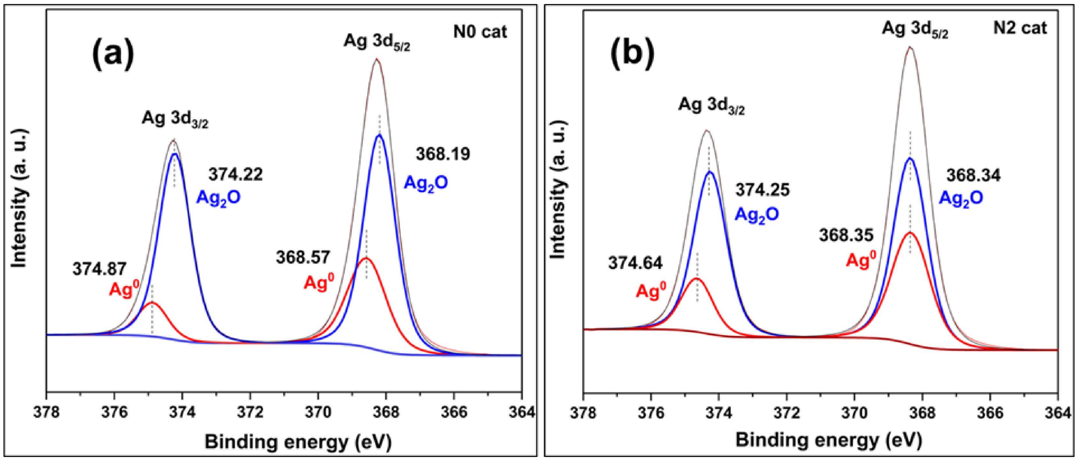

Figure 4.7 Ag 3d deconvolution of (a) N0 and (b) N2 catalysts.

The deconvoluted Ag 3d peaks of N0 and N2 (Figure 4.7) showed that there is a presence of Ag^0 along with Ag^{1+}. The percentage of Ag^0 increased with Ni-doping (see Table 4.2). As mentioned earlier, the XRD of the N2 sample also shows evidence of FCC Ag formation. Thus, Ag^0 is formed to charge-compensate for the oxygen vacancy.

Table 4.2 The Ag^0 and Ag^{1+} percentage from the deconvolution of Ag 3d for the N0 and N2 catalyst samples.

Sample	**Ag^0 (%)**	**Ag^{1+} (%)**
N0	25.88	74.13
N2	34.09	65.92

Note that Ag^0 is not part of the Ag_2O matrix. After considering this factor, the (Ag_2O lattice) O_L+O_V oxygen ratio to Ag^{1+} is ~0.435 in the N0 sample. Similarly, the (Ag_2O lattice) O_L+O_V oxygen to Ag^{1+} ratio in the N2 sample is ~ 0.505. Figure 4.9 gives the high-resolution deconvoluted spectrum of the Ni 2p peak.

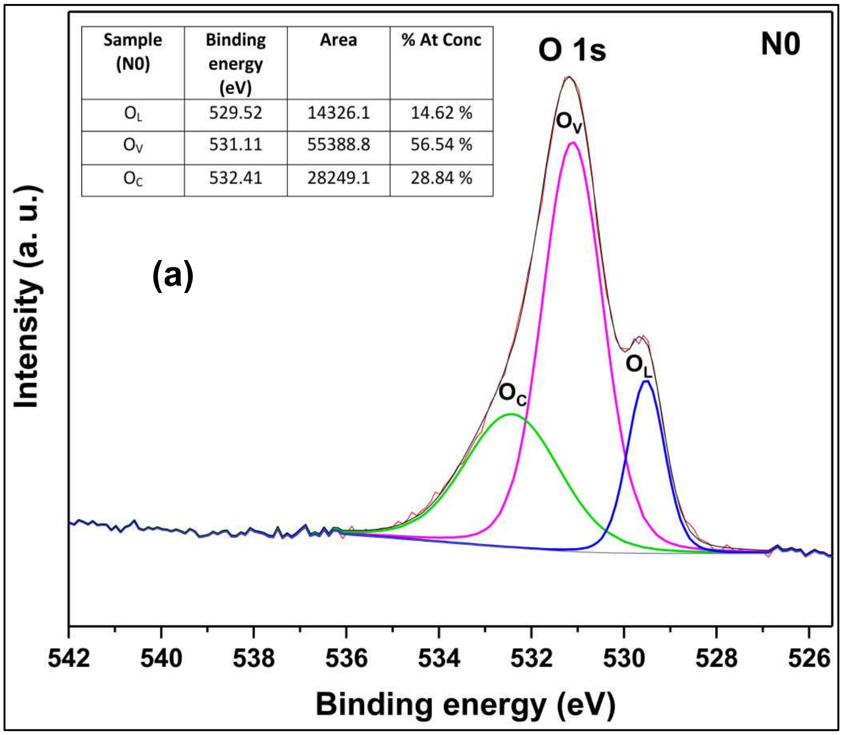

Sample (N0)	Binding energy (eV)	Area	% At Conc
O_L	529.52	14326.1	14.62 %
O_V	531.11	55388.8	56.54 %
O_C	532.41	28249.1	28.84 %

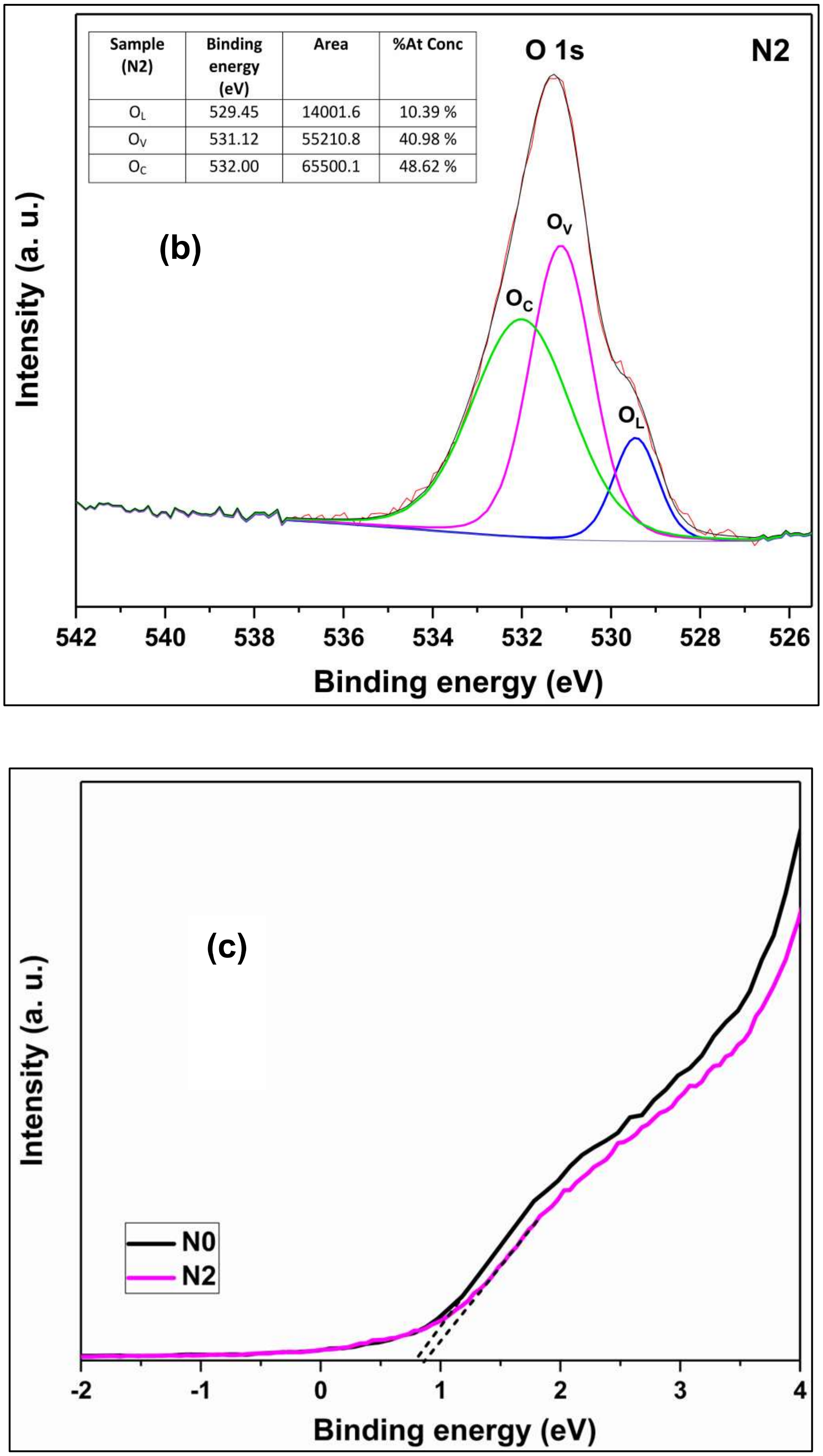

Sample (N2)	Binding energy (eV)	Area	%At Conc
O_L	529.45	14001.6	10.39 %
O_V	531.12	55210.8	40.98 %
O_C	532.00	65500.1	48.62 %

Figure 4.8 (a) O 1s peak deconvolution of the N0 sample (b) O 1s peak deconvolution of the N2 sample (c) the XPS valence band spectra of N0 and N2 sample.

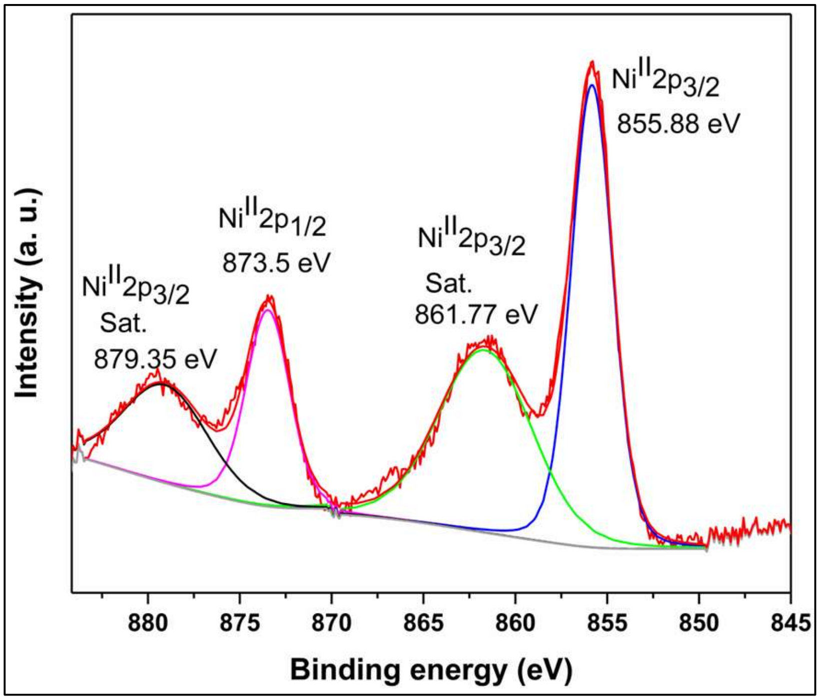

Figure 4.9 Deconvoluted XPS spectra of Ni 2p for N2 sample.

The bandgap from UV-visible diffuse reflectance spectroscopy (UV-DRS) (Figure 4.10) and valence band XPS (VB-XPS) information were combined to find the VB and CB positions of N0 and N2 samples.

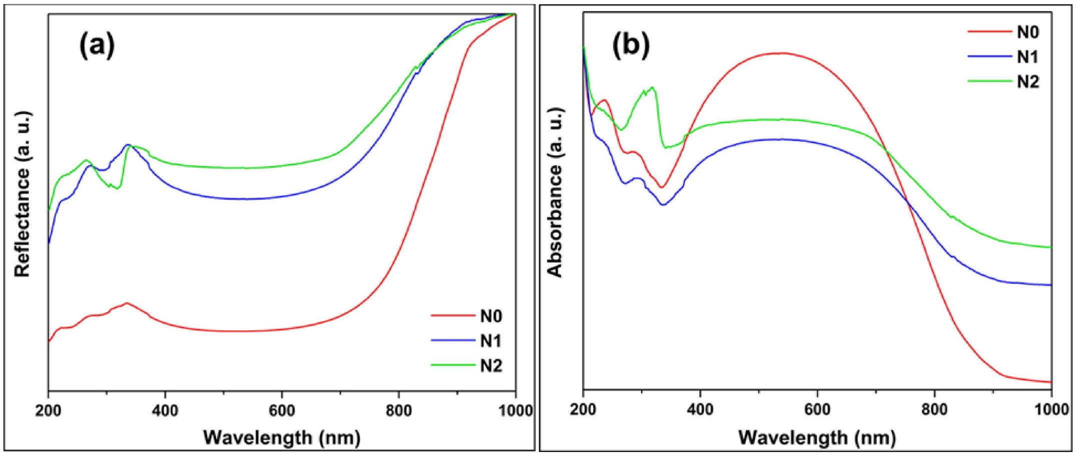

Figure 4.10 (a) UV-Vis reflectance and (b) UV-Vis absorbance spectra of N0, N1, and N2.

Figure 4.11 shows the Tauc plot obtained from the UV-DRS absorption data of the samples. The tangent of the linear part of the curve cuts the x-axis and implies the materials' bandgap energy value (eV). Samples N0, N1, and N2 display the bandgap values 1.53, 1.43, and 1.4 eV, respectively. The bandgap decreases with Ni doping. N2 has the least bandgap (1.4 eV) among the three samples. Figure 4.8c shows the VB-XPS spectra of the N0 and N2 samples. VB-XPS revealed the VB position of the samples. As shown in the Figure (Figure 4.8c), the x-axis intercept represents the VB positions i.e. for N0 = 0.8 eV and for N2 = 0.87 eV. The VB position of N2 is slightly shifted to a more positive value than N0. The CB edges of samples N0 and N2 are at -0.73 and -0.53 eV, respectively. The CB of the N2 sample gets shifted (by 0.2 eV) more than the N0 sample. Moreover, the CB shift is more than the VB shift.

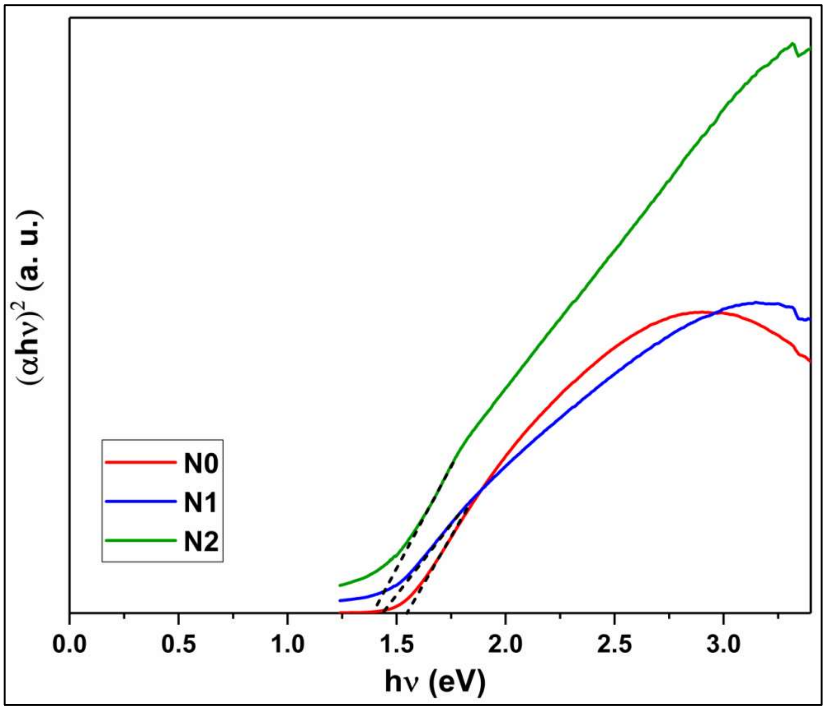

Figure 4.11 The Tauc plots of samples N0, N1, and N2.

4.3.3 Photoluminescence Study

An analysis of the nanoparticle samples' photoluminescence (PL) spectrum gives information about their relative recombination efficiencies (of holes and electrons) on photo-excitation. Delayed recombination causes decreased PL intensity and, consequently, better photocatalytic efficiency (De et al., 2020; Jatav et al., 2021; U. Kumar et al., 2021). Figure 4.12 displays the PL spectra of the N0 and N2 samples. The intensity of the doped material PL spectrum is lesser than that of the sample N0. Hence, Ni-doping reduces recombination and improves charge separation. This result agrees with the XPS results that Ni-doping enhances charge density on the chemisorbed oxygen and facilitates effective charge separation (Z. Cui et al., 2019).

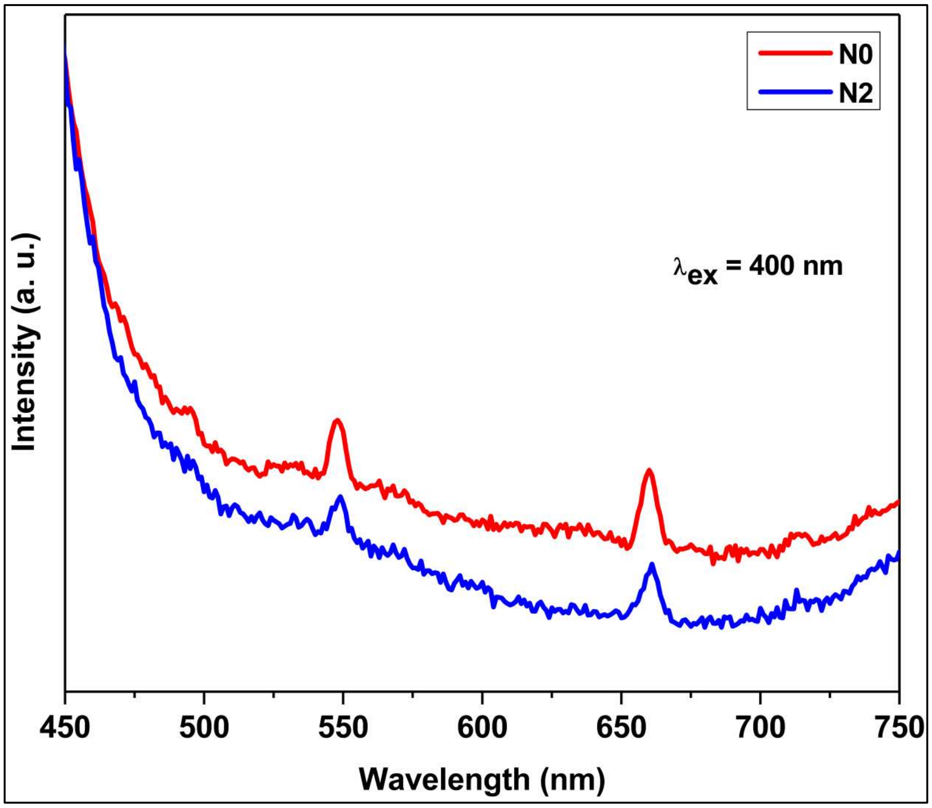

Figure 4.12 PL spectra of N0 and N2 samples.

4.3.4 DFT calculations

This sub-section elaborates the results of DFT calculations to understand better the Ni-Ag_2O system electronic structure with and without oxygen vacancies. As mentioned earlier, initially, the formation energy of the Ag_2O system was calculated. Then two Ni-doped Ag_2O model systems were designed. One had an Ag substituted by a Ni atom and, in another, the Ni atom occupied an interstitial position. The formation energy of the substituted Ni-doped Ag_2O system was 0.18 eV, while that of the interstitially doped system was 1.09 eV. Thus, energy-wise, the substitutional Ni-doped defect in the Ag_2O system is considerably more favorable and agrees with the earlier discussed HR-XRD finding.

We introduced oxygen vacancy in the pure Ag_2O supercell to analyze the OV's contribution to the material's electronic band structure. Figure 4.13a compares the DOS of the pure Ag_2O and OV-rich Ag_2O. OV-rich Ag_2O generates a finite bandgap of 0.5 eV, whereas the pure one gave approximately zero bandgap due to the widely reported DFT calculation bandgap under-evaluation (Allen et al., 2011). As shown in the Figure inset, the flat portion of OV Ag_2O represents the material's bandgap. Ni dopant inclusion in the OV-rich Ag_2O system introduced a new dopant level in the bandgap region. Because of the dopant level, the DFT calculations again gave an underestimated zero bandgap for the Ni-doped OV-rich Ag_2O system.

The Ni dopant levels are around the Fermi level (shown in the inset of Figure 4.13b) region. Most importantly, the effective CB region (from CB minimum to CB maximum) shifted from 9.8 eV to 6.7 eV, while the VB electron density shifted from -6.7 eV to -6.9 eV. Therefore, the CB shift is much more than that observed for VB in the Ni-doped OV-rich Ag_2O system. Note that this shift in VB and CB positions is qualitatively analogous to the VB-XPS observations.

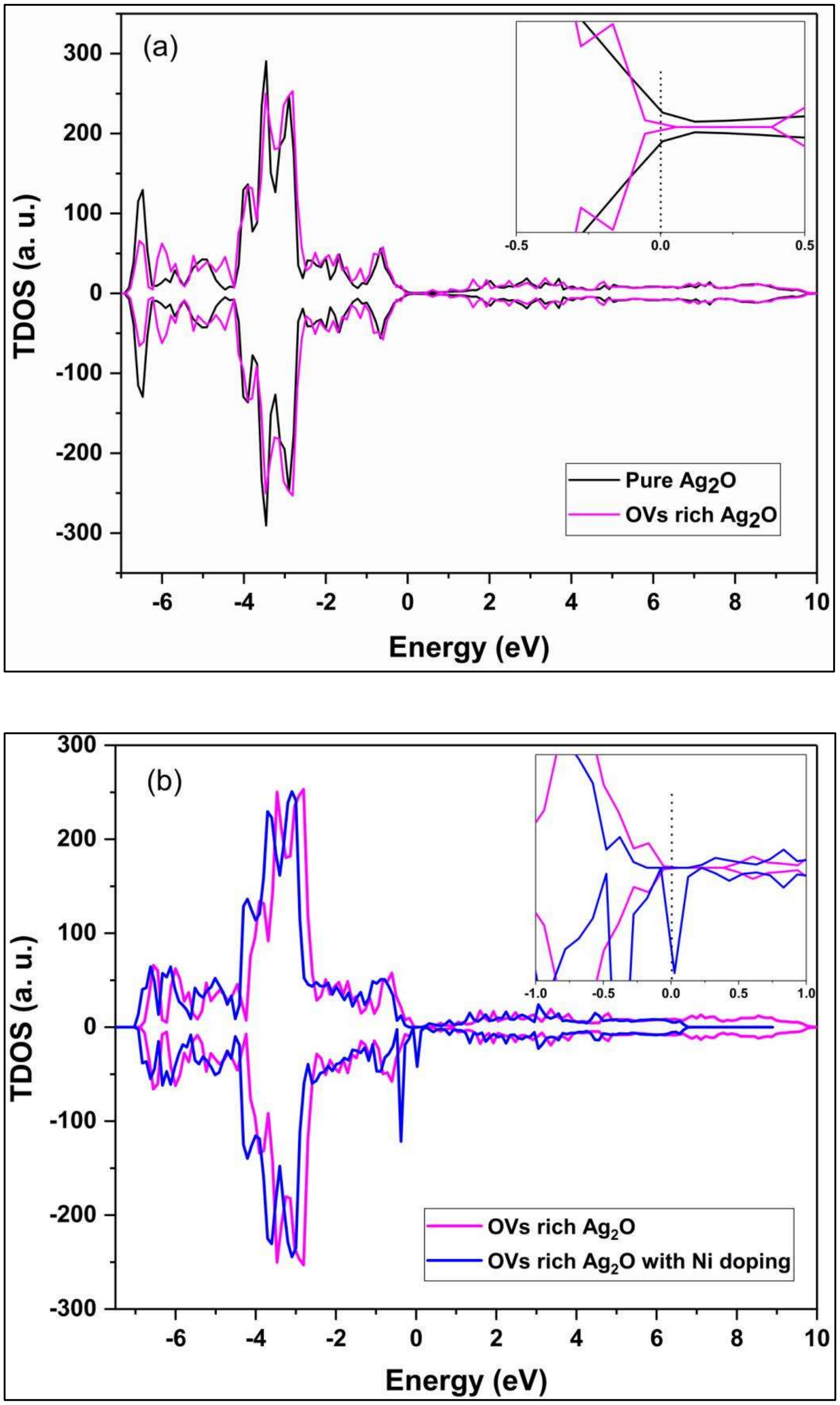

Figure 4.13 (a) A comparison of the total density of states (TDOS) of the pure Ag_2O and OV-rich Ag_2O (b) Comparison of the total density of states (TDOS) of OV-rich Ag_2O and Ni doping.

4.3.5 Photocatalytic efficiency assessment

The photocatalytic degradation of CIP was performed under visible light irradiation over samples N0, N1, and N2. Figure 4.14a displays the effect of visible light irradiation on CIP degradation with time. The Figure shows plots for experiments done both in the absence and presence of a photocatalyst. No CIP degradation took place in the absence of a photocatalyst (blank experiment). CIP degradation occurred only when a photocatalyst was present in the reaction mixture. The rate of photocatalytic degradation increased with Ni doping in Ag_2O. Thus, N2 exhibited the best CIP degradation photocatalytic activity. We tested the CIP degradation data for zero, first, and second order kinetics. The CIP degradation best fitted the first-order kinetics. Figure 4.14b shows the variation of $-\ln(C/C_0)$ with the irradiation time as per the equation below.

$$-\ln(C/C_0) = k_{app}t$$

Here, C is the CIP concentration at time t. C_0 is the initial concentration of CIP and k_{app} is the apparent rate constant. The apparent rate constants found from the fits were 0.0119 min^{-1} for N0, 0.0141 min^{-1} for N1, and 0.0212 min^{-1} for N2. Clearly, the N2 catalyst shows better catalytic activity on CIP degradation. But apparent rate constants are not comparable for different experiments because of the different amount of catalysts or the reaction kinetics orders. Therefore, turnover frequencies (TOF) were also calculated. Table 4.3 presents these values. The TOF units for data given in the table are $mol.g^{-1}.min^{-1}$ since the catalysts are not stoichiometric.

Table 4.3 Turn over frequency values of the un-doped and doped catalysts.

Catalysts	The apparent rate constant (min^{-1})	TOF (mole $g^{-1}min^{-1}$)
N0	0.0119	4.59×10^{-6}
N1	0.0141	5.12×10^{-6}
N2	0.0212	6.55×10^{-6}

The active species involved in the photocatalytic degradation were found by conducting scavenging experiments specific to holes (h^+), superoxides ($O_2^{\cdot -}$), and hydroxyl ($^{\cdot}OH$) radicals with the N2 catalyst. Para-benzoquinone (PBQ), potassium iodide (KI), and isopropyl alcohol (IPA) were used to scavenge $O_2^{\cdot -}$, h^+, and $^{\cdot}OH$ radicals, respectively. The results show that holes and superoxides are the main active species affecting photocatalytic CIP degradation (Figure 4.14c). Figure 4.14d displays the results of the recyclability experiments for CIP degradation with the N2 photocatalyst. The first use of the N2 photocatalyst gave almost 58% CIP degradation, and it exhibited good recyclability up to the fourth cycle.

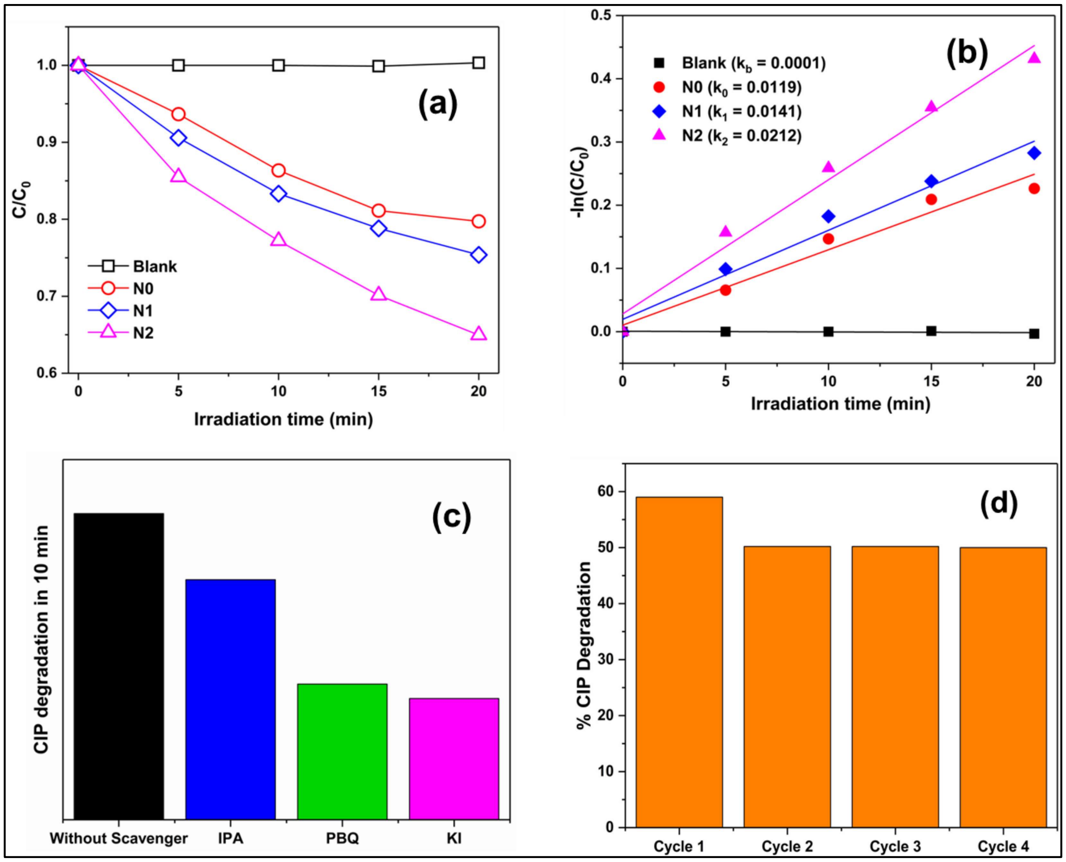

Figure 4.14 (a) UV-Vis absorption spectra of photocatalytic degradation of CIP with undoped (N0) and doped catalysts (N1 and N2) (b) The variation of –ln(C/C_0) as a function of irradiation time (c) Trapping experiments for CIP degradation on N2 photocatalyst (d) reusability plot of N2 photocatalyst.

4.3.6 Proposed mechanism

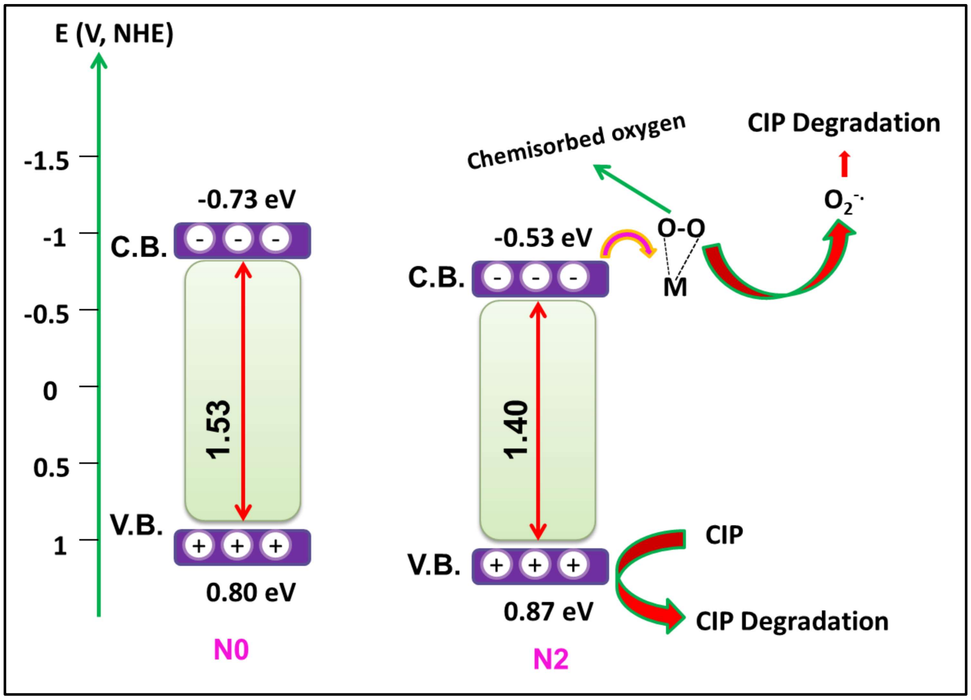

Figure 4.15 Schematic of the proposed CIP photo-degradation mechanism.

DFT calculations and XPS analysis demonstrate that OVs are responsible for widening the bandgap (1.53 eV) of Ag_2O nanoparticles. Ni doping in OV-Ag_2O systems decreases the bandgap to 1.4 eV and also shifts the VB and CB band positions. A crucial observation is that about 29% chemisorbed oxygen is present in N0, along with OVs. Surface OVs are sites for the chemisorption of oxygen (M. Li et al., 2021; Marikutsa et al., 2021). Furthermore, chemisorbed oxygen increased in N2. The +2 oxidation state of the dopant Ni is higher than that of Ag in Ag_2O. Hence, such doping introduced excess electrons into the system. Ni dopants on the nanoparticle surface increased the chemisorbed oxygen to 48% of the total oxygen.

Figure 4.15 gives the schematic diagram of the proposed photocatalytic CIP degradation mechanism. On irradiation of the photocatalyst with visible light, electrons were photo-excited from its VB to the CB. OVs can trap such photo-excited electrons and transfer them to chemisorbed oxygen. This results in the formation of superoxide radicals and, consequently, other reactive oxygen species. The reactive species trapping experiments tell us that superoxide radicals and holes affect the reaction rate almost equally. The VB position of the photocatalyst is also vital. Since N2 has a more positive VB position than N0, oxidation of CIP through holes is also more effective. Additionally, sample N2 has more chemisorbed oxygen, resulting in a higher superoxide production rate.

4.4 Conclusions

Ag_2O nanoparticles fabricated by a hydrothermal methodology exhibited a 1.53 eV bandgap. XPS analysis and DFT calculations revealed that OVs in these nanoparticles caused the enlarged bandgap. Furthermore, the prepared Ag_2O nanoparticles also had chemisorbed oxygens. Valence band XPS also showed that these Ag_2O nanoparticles had a negative CB position. An equivalent hydrothermal procedure, with an additional step of Ni salt solution addition at an appropriate juncture, led to the synthesis of Ni-doped Ag_2O nanoparticles. XRD results and DFT calculations showed that the Ni atoms had substituted Ag in the doped Ag_2O system with a slightly contracted lattice.

Doping with Ni decreased OVs in the nanoparticles but increased the chemisorbed oxygen percentage due to the injection of additional electrons. Lesser OVs resulted in relatively smaller bandgaps in the Ni-doped samples. Compared to the OV-mediated Ag_2O nanoparticles, a valence band XPS analysis showed that these samples had a less negative CB and a more positive VB. DFT calculations on a Ni-doped Ag_2O model with an OV also demonstrated qualitatively similar results. The photocatalytic activities of OV-mediated and Ni-doped Ag_2O nanoparticles were evaluated for ciprofloxacin (CIP) degradation. Ni-doped systems exhibited faster CIP degradation. A more positive VB position and higher chemisorbed oxygen percentage led to increased CIP degradation due to oxidation on generated holes and enhanced superoxide radical formation. It seems dopants that can increase the supply of excess electrons to a metal oxide can increase chemisorbed oxygens on its surface.

CHAPTER 5: S doped Ag_2O photocatalysts

5.1 Introduction

Photocatalysis is a green and economical process that can resolve the current energy and environmental issues (Melchionna & Fornasiero, 2020; Molinari et al., 2020; J. Yu et al., 2012). This technique suffers from two significant issues. One is the rapid recombination of photo-generated electrons and holes pair after photo-excitation of the photocatalyst, resulting in lesser photocatalytic activity of the semiconductor material. Effective charge separation and appropriate adsorption of the targeted redox species on the photocatalyst can reduce this recombination problem. The second requirement for an efficient photocatalyst is having suitable conduction band (CB) and valence band (VB) positions. CB and VB should be above and below the reduction and the oxidation couple, respectively. Photocatalysis research demands semiconductor nanostructures with appropriate band structures that ensure charge separation and strong redox driving forces (Jatav et al., 2021; S. Kumar et al., 2019; U. Kumar, Das Chakraborty, et al., 2022; U. Kumar, Kuntail, et al., 2022; Pal et al., 2022).

Introducing defects like vacancies or dopants in the parent semiconductor material can increase charge separation and alter the bandgap and adsorption properties. For instance, Hezam et al. synthesized oxygen vacancy (OV) enriched ceria (CeO_2) with better charge separation and enhanced photocatalytic activity (Hezam et al., 2020). OV-generated defect sites can trap the photo-induced excited species to improve the charge carrier separation. Surface defects are also adsorption sites for the desired reactant. Furthermore, OVs and (cation or anion) doping also modify the electronic band structure of the parent semiconductor (Gleditzsch et al., 2019; Hirai et al., 2020; Mitra et al., 2012; Serpone, 2006; Tang et al., 2018a). The dopant's orbitals may be introduced between the CB and VB or hybridized with pure analog orbitals (De et al., 2020; J. Zhao et al., 2020). Therefore, the semiconductor's bandgap can be widened or narrowed down depending on the nature of the defect.

Doping is also crucial in the context of the creation of OV defects (Chu et al., 2020; X. Li et al., 2018). The oxidation state of the dopant or its size can induce OVs. Doping by lower valent cations makes the semiconductor electron-deficient, and OVs are created to correct the resultant charge imbalance. For example, WO_3 (the oxidation state of W is +6) doped with Cr^{3+} resulted in OV formation for local charge compensation (F. Li et al., 2018). The adsorption behavior of the nanomaterials also changed due to such doping (K. V. Kumar et al., 2015; M. Liu, 2020; Zhong et al., 2013). High-pressure synthesis methods like solvothermal synthesis can also induce OV creation. Elevated pressure conditions balance the strains in the crystal lattice due to OV formation (Y. Huang et al., 2019; T. Liu et al., 2015; Jiaqi Zhang & Li, 2022). The lattice distortion strains due to substitution by larger anions can also cause OV formation (Gomez et al., 2020).

The visible range constitutes a significant portion of the solar spectrum. Small and moderate bandgap visible-light photocatalysts can efficiently use this visible range radiation. Ag_2O is a narrow bandgap semiconductor (1.2 - 1.5 eV) that can use a large part of the UV-visible spectrum. But the small bandgap also means that its VB or CB position may not be appropriate for the desired redox reaction. Pure Ag_2O photocatalysts also suffer from photo-stability and recombination issues (Gomez et al., 2020). Doping can widen this bandgap and give better charge separation for enhanced photocatalytic activity. For instance, Zn or Sr doped Ag_2O exhibits a wider bandgap (De et al., 2020; Kiani et al., 2019). As mentioned earlier, doping also modifies the adsorption properties of the parent semiconductor, affecting the photocatalytic activity towards a target reactant. While density functional theory (DFT) calculations have predicted that oxygen vacancies will widen the Ag_2O bandgap, no validating experimental reports in literature correspond to this prediction. Hence, potentially Ag_2O with doping and vacancy defects could effectively be a new photocatalyst with better activity.

An extensive literature survey reveals very little photocatalysis research on developing such doped Ag_2O photocatalysts. Given the above perspective, the present study focuses on the change in structural and electronic properties of Ag_2O nanoparticles induced by sulfur (S) doping. Note that the structural and electronic properties of such S-doped Ag_2O have not been studied previously. Furthermore, S as a dopant can exhibit variable oxidation states (+6, +4, and -2); therefore, it is possible to generate charge imbalance in the Ag_2O system. Different sizes and charges of the dopant species can cause OV defects and change the electronic properties of the doped system.

Given the narrow bandgap of pure Ag_2O, the priority was to find whether S-doping could increase the material's bandgap. We conducted DFT calculations on several models with sulfur substituting oxygen or occupying an interstitial position with or without oxygen vacancies. The qualitative results indicated that sulfur substitution could widen the bandgap relative to the undoped one. Based on this prediction, experimental preparation of S-doped Ag_2O nanoparticles was conceived. The dopant mole percent was kept at a very low level ($\leq 1.25\%$) to prevent (S- based) the formation of compounds like Ag_2S, Ag_2SO_3, and Ag_2SO_4. A hydrothermal protocol was used to prepare pure and S-doped Ag_2O. X-ray diffraction (XRD) analysis demonstrated that S doping contracted the crystal lattice. X-ray photoelectron spectroscopy (XPS) investigation detected oxygen vacancy formation in undoped and doped Ag_2O nanoparticles. The photoluminescence studies investigated the relative recombination efficiencies. The DFT calculation results combined with XRD and XPS analysis evidence led to the possible dopant position in the Ag_2O crystal lattice. Under visible light irradiation, the prepared S-doped Ag_2O nanoparticles exhibited enhanced photocatalytic activity towards RhB degradation. Experiments with scavenger molecules determined the active species responsible for photocatalytic activity. The collated information from various investigations led to the probable photocatalytic mechanism.

5.2 Experimental

5.2.1 Sample preparation

Synthesis of pure Ag_2O nanoparticles

Two millimoles (mmol) of $AgNO_3$ were dissolved in 40 ml DDDW water by continuous stirring for 15 minutes. Then, 0.2N NaOH was added dropwise into the previous solution. The addition of NaOH was continued until the pH of the reaction mixture reached 11. Then, the resulting mixture was transferred into a 100 ml stainless steel autoclave and heated in a hot-air oven at $180^{O}C$ for 24 hours. A black precipitate was formed. The precipitate was separated and washed several times with DDDW and ethanol. The end product was dried at $50^{O}C$ in a hot air oven to get the pure Ag_2O nanoparticles (denoted by B0).

Synthesis of sulfur-doped Ag_2O nanoparticles

Three different molar ratios of thiourea ($CS(NH_2)_2$) and $AgNO_3$ were used to synthesize three sulfur-doped Ag_2O (hereafter denoted by B1, B2, and B3) samples. The B1, B2, and B3 were prepared using 0.3, 1.25, and 2.5 mol% of thiourea. The first step was to dissolve the desired amount of $AgNO_3$ in DDDW water and adjust the solution pH to 11. Then, the required amount of thiourea solution was added to this solution, maintaining the final solution pH at 11. The reaction mixture was stirred for another 15 minutes and transferred to a 100 ml stainless steel autoclave for hydrothermal treatment at $180^{O}C$ for 24 hours. Synthesized materials were washed with DDDW and ethanol. This step was followed by drying at $50^{0}C$ in a hot air oven to get the doped samples.

5.2.2 Computational details

All the theoretical calculations were performed using plane-wave DFT in the Vienna ab-initio simulation package (VASP). The models for all the investigations were created on the Medea-VASP platform. DFT calculations were carried out using generalized gradient approximation Perdew-Burke-Ernzerhoff (GGA-PBE) exchange-correlation functional and the projected augmented wave (PAW) pseudopotential. Initially, a 2x2x2 supercell was built from the Ag_2O unit cell (Card No: COD 4318188) and optimized using a 2x2x2 k-point mesh size and 520 eV plane-wave basis set energy cut-off. This perfect Ag_2O model is labeled as C0 in the rest of this article. Taking C0 as the base model, two types of sulfur doping possibilities were investigated. In one case, an oxygen atom in this perfect Ag_2O supercell model was substituted by a sulfur atom (CP1). The second model had the dopant sulfur atom placed in an interstitial site of the supercell (CP2).

Four more Ag_2O models with O-vacancy and S-doping defects were also designed and investigated. All calculations on these defect models were carried out with the optimized parameters used for the C0 model. The first defect model considered was the Ag_2O supercell with an O-vacancy (hereafter denoted by C1). In the second model, an S substituted an O in the C1 model (hereafter labeled as C2). This model, therefore, has an O-vacancy and oxygen substituted by sulfur. The third model (labeled as C3) introduced the dopant S atom in an Ag_2O crystal interstitial position in the C1 prototype. Figure 5.1 shows the schematic of the C0, C1, and C2 models. Then, the S-doped formation energies of the respective systems were computed as per equations (5.1) and (5.2).

$$E_f(C2) = E_{defect}(C2) - [E_{C1} + \mu_S - \mu_O] \qquad (5.1)$$

$$E_f(C3) = E_{defect}(C3) - [E_{C1} + \mu_S] \qquad (5.2)$$

Here E_f *(C2)* and E_f (*C3*) represent the formation energies of C2 and C3 systems, respectively. The chemical potentials of S and O are denoted by μ_S and μ_O. The μ_O and μ_S were defined as energy per oxygen and sulfur atom from the O_2 (COD 2106877) and $(S_8)_4$ (COD 2002079) unit cells, respectively (X. Xiang et al., 2015). In addition, the density of states (DOS) of these models was collected from the optimized supercells by single point calculation using 8 × 8 × 8 K mesh and 400 eV energy cut-off value.

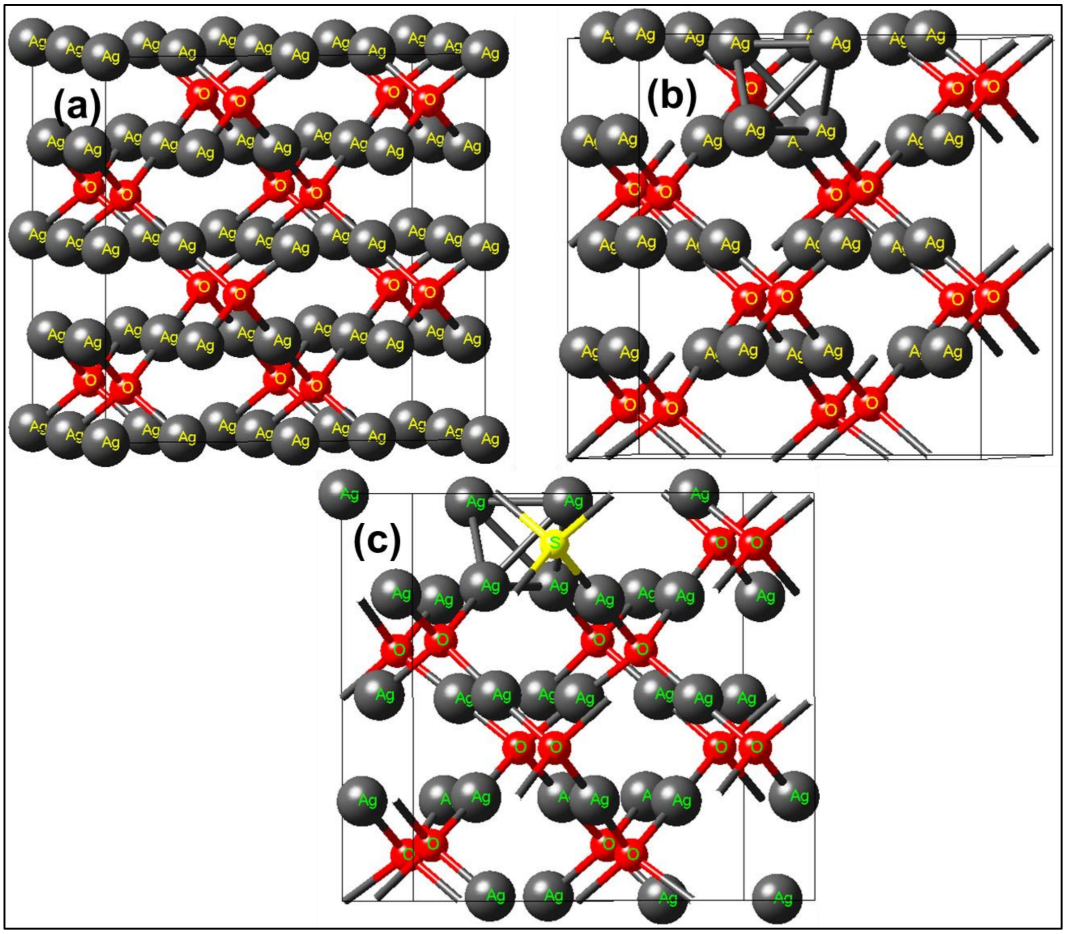

Figure 5.1 Optimized geometry of C0, C1, and C2 models.

5.2.3 Photocatalysis experimental details

The photocatalytic activities of the prepared samples were evaluated for Rhodamine B (RhB) degradation under visible light irradiation. In a typical photocatalysis experiment, 2.3 ml RhB (3.5 mg/L) aqueous solution and 0.1 mg photocatalyst were mixed in a standard 4 ml quartz cuvette. Subsequently, 6uL of 0.1M HCl was added to maintain the reaction mixture pH at 3. The reaction mixture was stirred (in the dark) for 20 minutes to achieve an adsorption-desorption equilibrium. Then this reaction mixture was placed under visible light irradiation in a homemade photocatalytic chamber under a 14W Philips cool white LED bulb (720 W/m^2 intensity) visible light source. The absorption spectrum of the mixture was recorded at regular time intervals.

5.3 Results and discussion

5.3.1 Structural properties

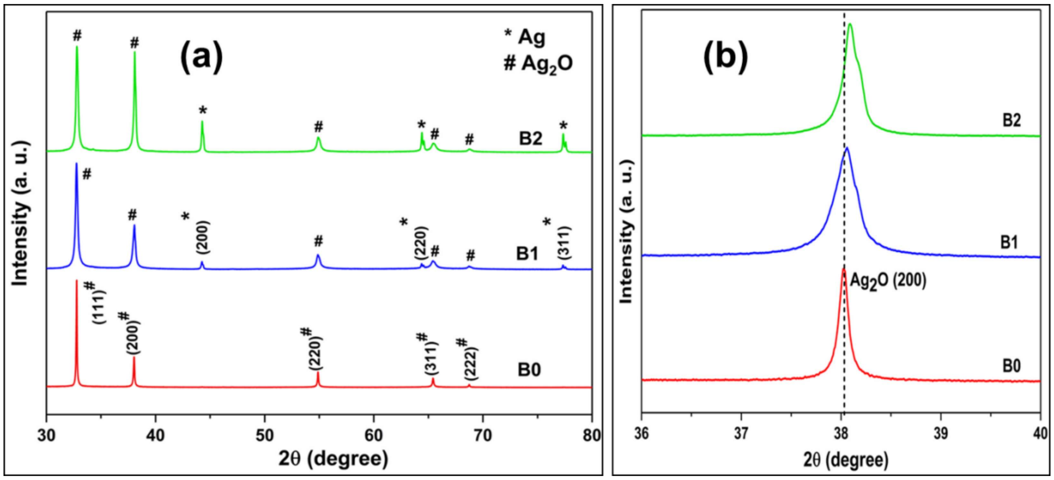

Figure 5.2 (a) Powder XRD patterns of the undoped and S-doped Ag_2O samples, (b) A comparison of the B0, B1, and B2 Ag_2O (200) plane XRD reflections (zoomed-in Ag_2O (200) peak).

Figure 5.2a displays the powder XRD patterns of undoped and S-doped Ag_2O nanoparticles. All peaks in the XRD of different samples match the standard FCC Ag_2O (JCPDS Card No. 75-1532) pattern. In addition, the doped samples (B1 and B2) also contain FCC Ag phases (JCPDS Card No. 89-3722). These XRD plots do not have any peak corresponding to Ag_2SO_4 or Ag_2SO_3 phases. Figure 5.3 shows the XRD pattern of the B3 sample with the highest S-doping (2.5 mol%) attempted. This XRD pattern has FCC Ag_2O, face-centered orthorhombic Ag_2SO_4 (JCPDS Card No. 80-1270), monoclinic primitive Ag_2SO_3 (JCPDS Card No. 70-1910), and orthorhombic Ag_2S phases. Since excess incorporation of sulfur causes phase separation into Ag_2SO_4, Ag_2SO_3, and Ag_2S phases (besides the parent Ag_2O structure), doping experiments with higher dopant mole percentages were not attempted (De et al., 2020). Therefore, the B3 sample was not used for any photocatalytic performance evaluations.

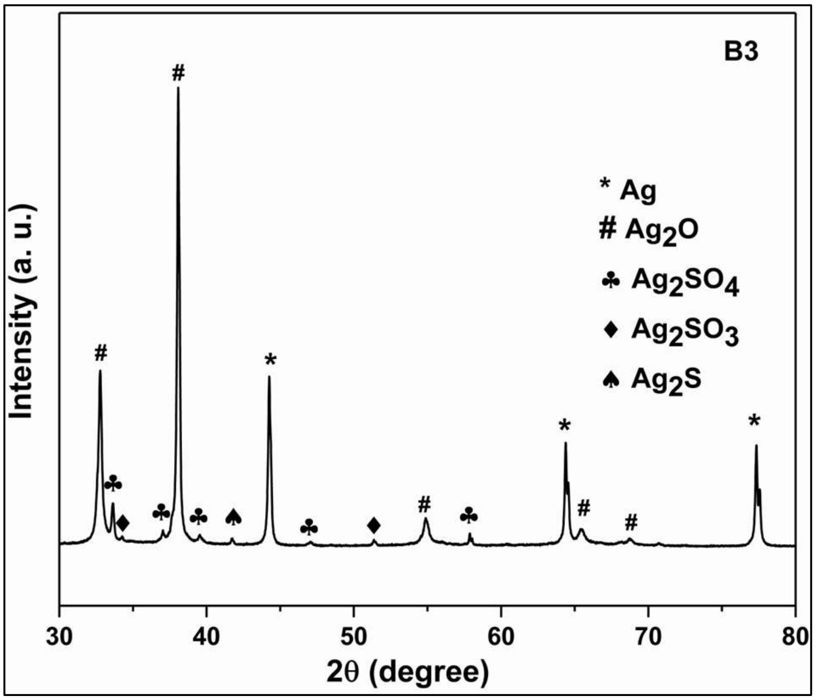

Figure 5.3 Powder XRD pattern of B3 sample.

Figure 5.2b compares the peak positions of the Ag_2O (200) plane for different samples. The diffraction peaks shift towards a higher Bragg's angle with an increasing dopant concentration. Thus, increased S-doping causes lattice contraction. The third column of Table 5.1 displays the lattice parameters of S0, S1, and S2 systems. Sulfur can exhibit -2, +4, and +6 oxidation states. But +4 and +6 oxidation states would entail the formation of Ag_2SO_3 and Ag_2SO_4 compounds/phases. Since these phases have not been formed, the reason for lattice contraction has to be different. One reason for the contraction of the Ag_2O lattice could be oxygen vacancies. This aspect is investigated in sub-sections 5.3.5 (XPS analysis) and 5.3.6 (DFT calculation results).

5.3.2 TEM and SEM analysis

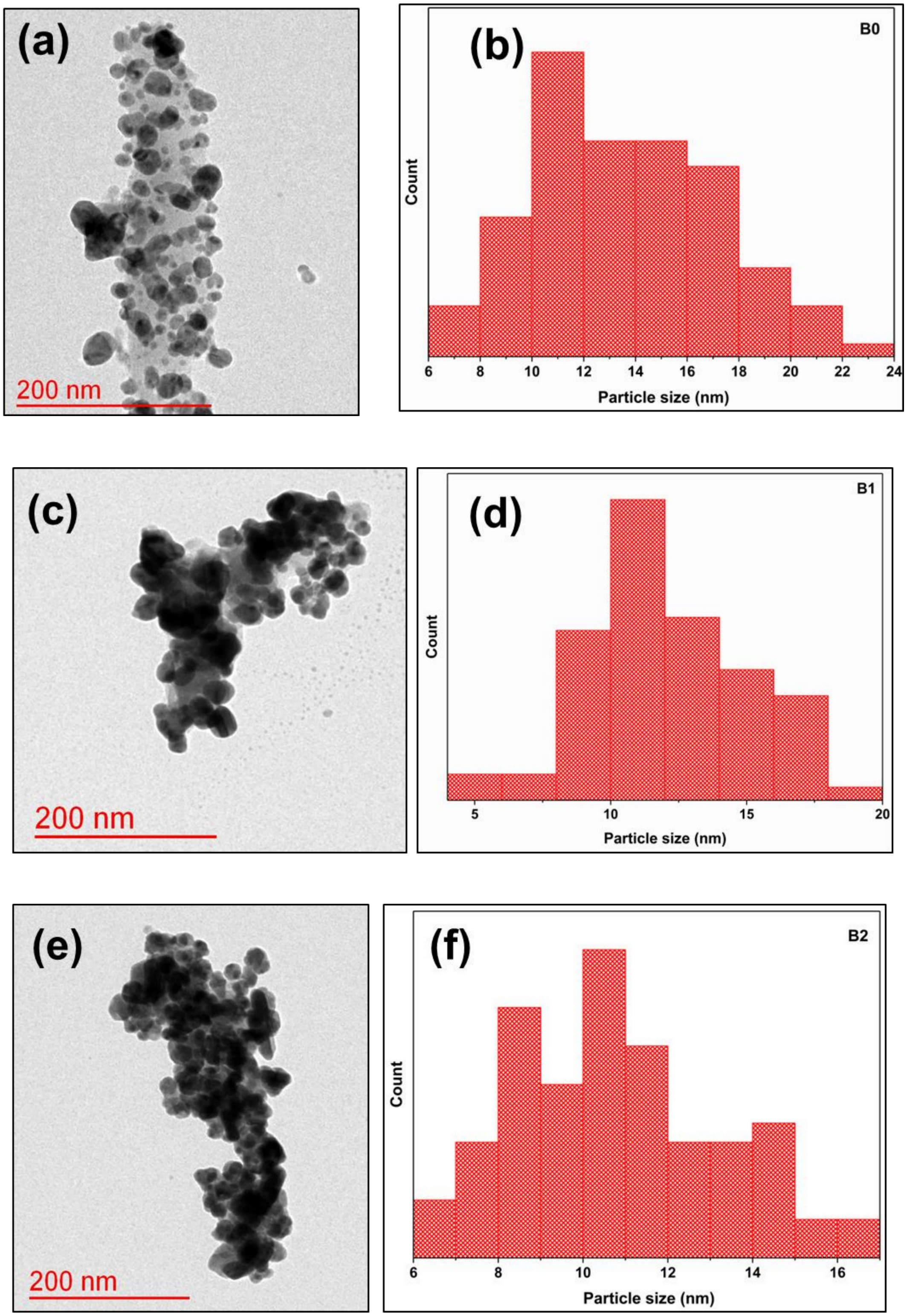

Figure 5.4 TEM images of B0 (a), B1 (c), B2 (e) and the particle size distribution of B0 (b), B1 (d), B2 (f).

TEM images give the shape and size of the prepared nanoparticles. Figure 5.4 displays the particle morphologies and size distributions of samples B0, B1, and B2, respectively. All synthesized nanoparticles are approximately spherical. Table 5.1 tabulates the synthesized nanoparticles' particle size and lattice parameter. Particle sizes decrease with the S doping. The incorporation of the dopant disrupts the regular symmetry of the pure crystal lattice (G. Xiang et al., 2015). Figure 5.5(a) and (b) display the high-resolution SEM images of B1 and B2 (doped samples). The respective elemental analysis tables are also attached with the corresponding images. This result indicates the presence of sulfur in all the doped samples.

Table 5.1 Variation in lattice parameter and average particle size with dopant concentration.

Dopant concentration (mole%)	**Particle size (nm)**	**Lattice parameter (Å)**
0	13.6	4.7292
0.3	12.1	4.7278
1.25	11	4.7214

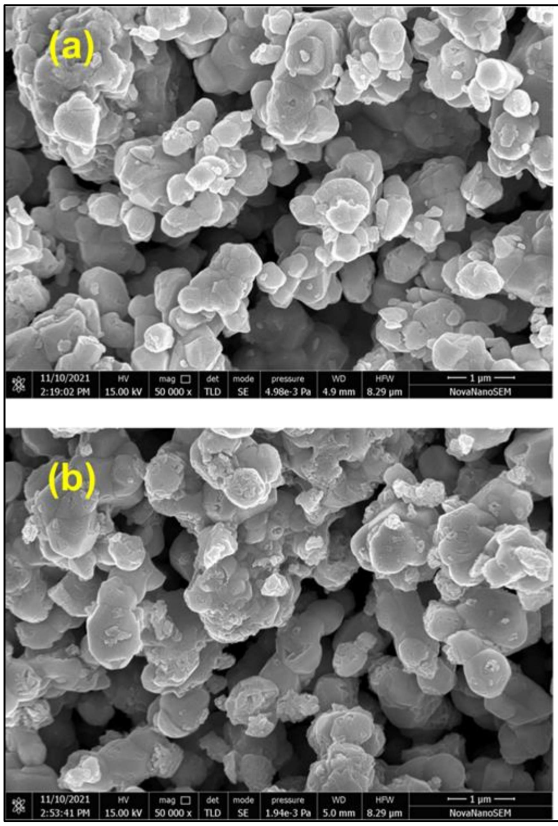

B1 sample

Element	Weight %	Atomic %
O K	3.09	17.36
S K	0.95	2.67
AgL	95.96	79.97

B2 sample

Element	Weight %	Atomic %
O K	2.48	14.23
S K	1.30	3.73
AgL	96.22	82.04

Figure 5.5 High-resolution SEM micrographs of (a) B1 and (b) B2 samples.

5.3.3 The bandgap

Figure 5.6a shows the solid-state UV-Vis absorption spectra of the samples prepared in this study. Equation (5.3) gives the Tauc relation for finding the bandgap of the as-prepared nanomaterials.

$$(\alpha h\nu)^{\frac{1}{n}} = h\nu - E_g \tag{5.3}$$

The bandgap is denoted by E_g, α represents the absorbance, h is the Plank's constant, and ϑ is the frequency. When n = ½, the graph is for the indirect bandgap, and n = 2 represents the direct bandgap plot. The x-axis intercept of the linear fit to the constant slope region of this plot gives the material bandgap (depicted in Figure 5.6b). The bandgaps of B0, B1, and B2 are 1.53, 1.70, and 1.89 eV, respectively. Thus, the bandgap increased with the dopant concentration.

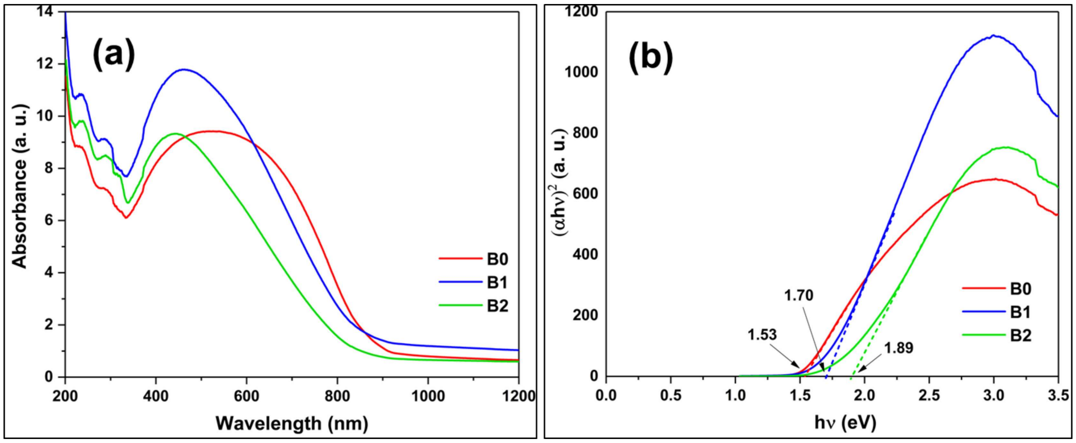

Figure 5.6 (a) The solid-state UV-visible absorption spectra and (b) Tauc plots of B0, B1, and B2 samples.

5.3.4 Photoluminescence studies

The emission (fluorescence) intensity can analyze the relative recombination efficiency. Lower intensity points to a slower recombination process and thereby improves charge separation. Figure 5.7 presents a comparison of PL spectra of doped nanomaterials with the undoped ones. The doped materials show lower intensity in comparison to the undoped analog. For the B2 sample, the intensity is the least. As reported in section 5.3.7, the B2 sample shows the maximum photocatalytic activity among the investigated samples.

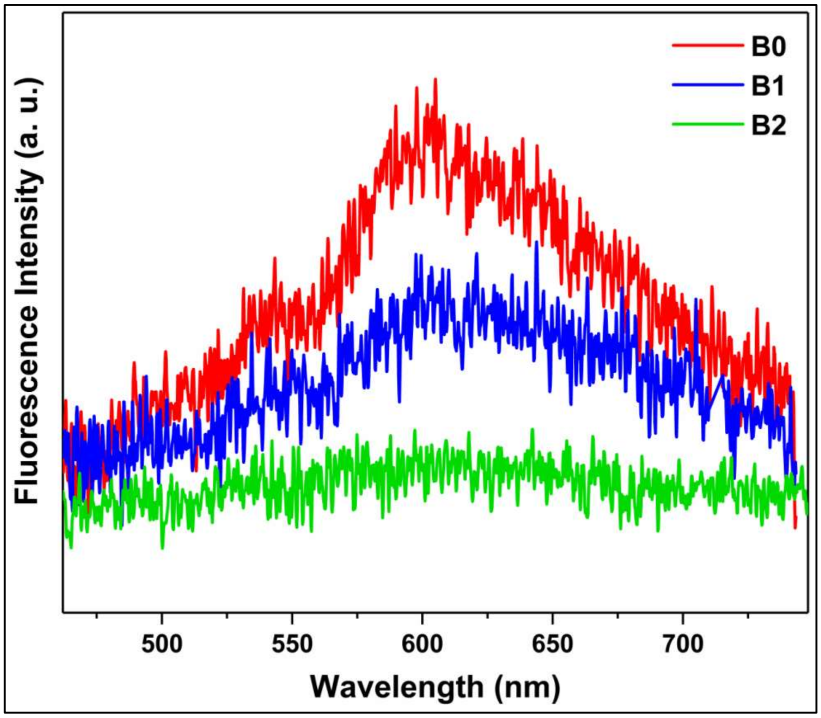

Figure 5.7 A comparison of the PL spectrum of B0, B1, and B2 samples.

5.3.5 XPS analysis

Figure 5.8 represent the survey XPS spectra of undoped (B0) and doped (B2) samples. The integration of the S2p peak area shows 0.97 atom percent of sulfur on the B2 surface. Furthermore, the O/Ag atomic concentration ratio is 0.476, less than 0.5.

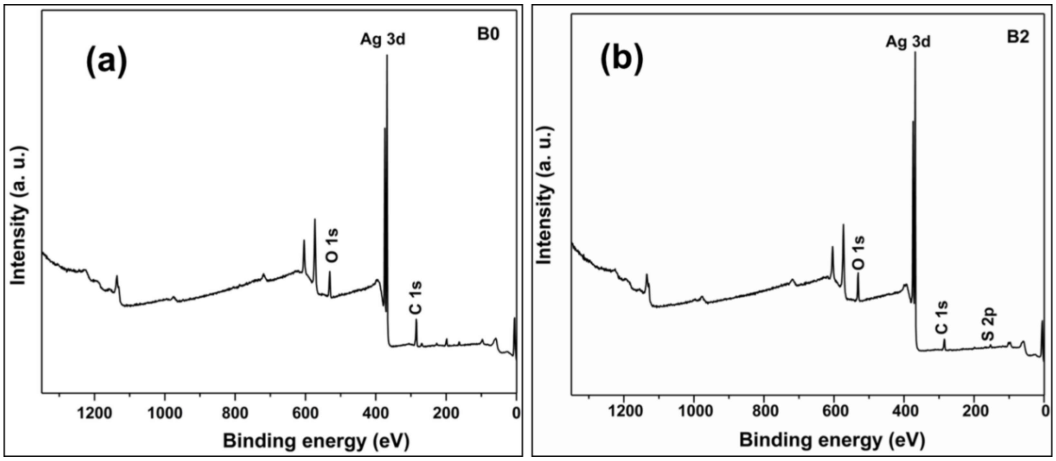

Figure 5.8 XPS survey spectrum of (a) B0 and (b) B2 samples.

The O1s spectrum was deconvoluted to estimate the various oxygen species in these nanomaterials. Figure 5.9 (a,b) displays the high-resolution O1s XPS spectra of the B0 and B2 samples. The deconvolution of O1s peak gives chemisorbed oxygen (O_C), lattice oxygen (O_L), and oxygen vacancy (O_V) regions. Different colors highlight these regions in the O1s curve. Both B0 and B2 O1s peaks showed significant areas under the O_V curves. But the B2 sample O_v curve area is substantially higher and thus implies more oxygen vacancies. Thus, S-doping increases the OV percentage. Note that the O_V region in the deconvoluted O1s peak represents oxygens neighboring the vacancies in the anion sub-lattice. These oxygens have coordination dissimilar to the perfect Ag_2O case (Gao et al., 2017). Sample B2 also exhibits significant Ag^0 formation (see XRD in Figure 5.2a). Oxygen vacancies leave excess electrons in the lattice, and these are used to form Ag^0. Furthermore, the B2 O_C percentage is substantially lesser than B0.

When sulfur goes into the Ag_2O lattice, it could be in +6, +4, or -2 oxidation states. The deconvolution of S 2p (shown in Figure 5.9c) high-resolution peak shows that sulfur in all three oxidation states is present in the B2 sample. Most sulfur is in the +6 oxidation state, while a relatively small part is in the -2 oxidation state. Figure 5.10 compares the Ag 3d XPS spectra of the B0 and B2 samples. Doping shifts the $3d_{5/2}$ and $3d_{3/2}$ peaks to lower binding energy values. It seems that S-doping causes charge transfer to the Ag part and decreases its binding energy.

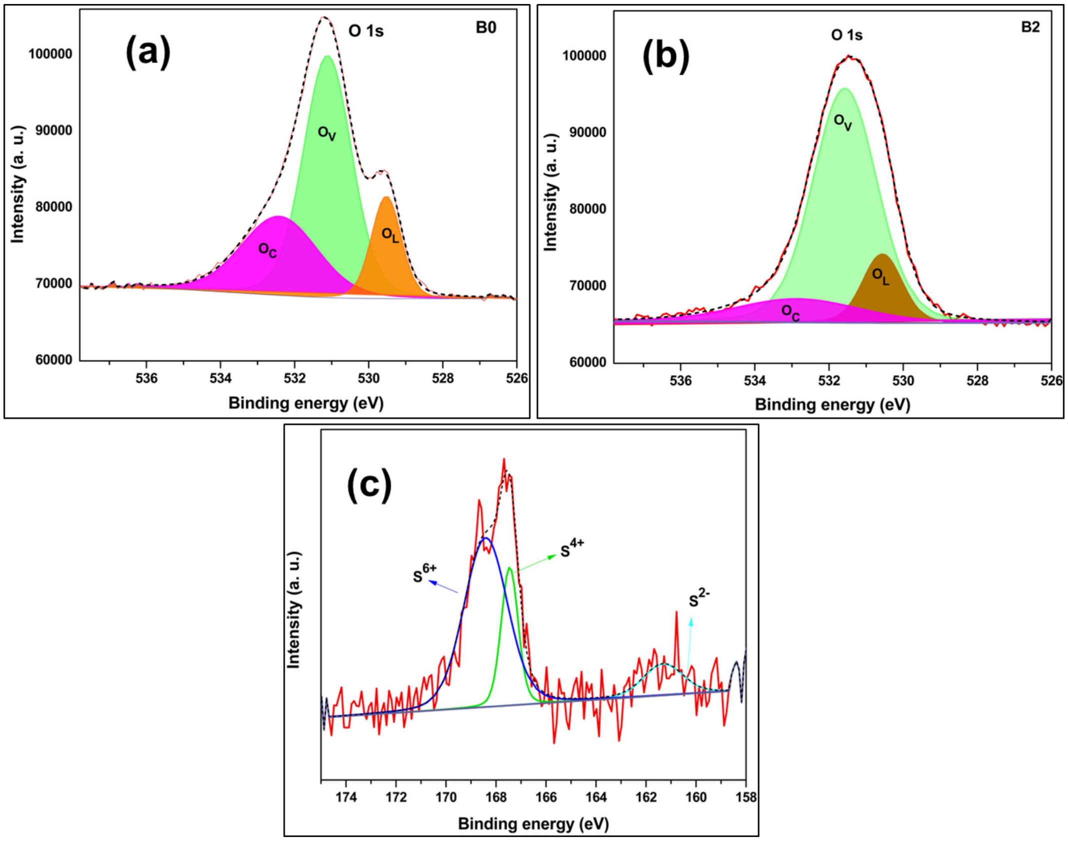

Figure 5.9 High resolution XPS spectrum of O 1s for (a) B0 and (b) B2 samples (c) high resolution XPS spectrum of S 2p for B2 sample.

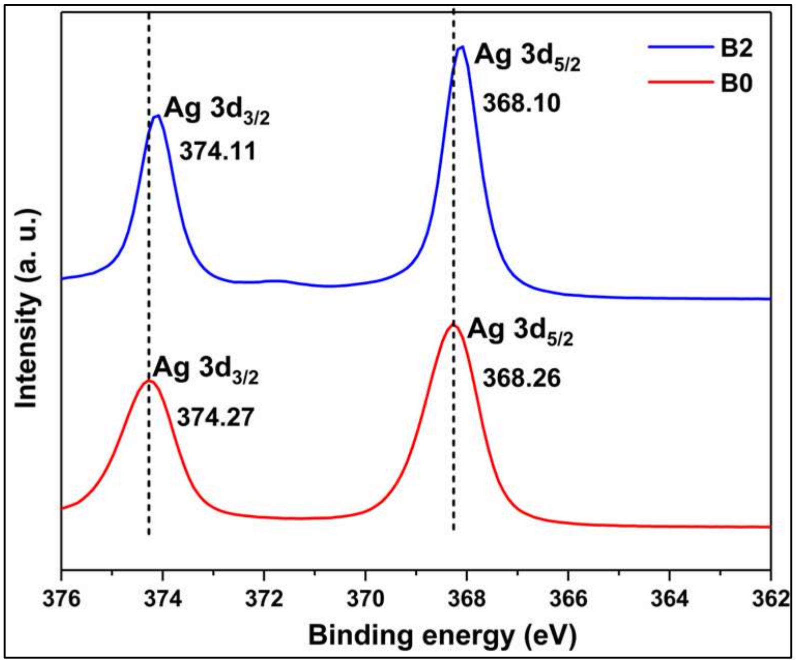

Figure 5.10 Comparison of high-resolution XPS spectrum of Ag 3d for undoped (B0) and doped (B2) Ag_2O.

Furthermore, the combination of UV-DRS and valence band XPS (in Figure 5.11) was used to obtain the VB and CB positions of the prepared nanoparticles. Table 5.2 displays the VB and CB positions (from VB-XPS) of the Ag_2O (doped and undoped) samples prepared in this study. The VB and CB positions of B2 are located at -0.46 and -2.35 eV. Compared to B0, sulfur-doped samples exhibit a significantly negative VB value.

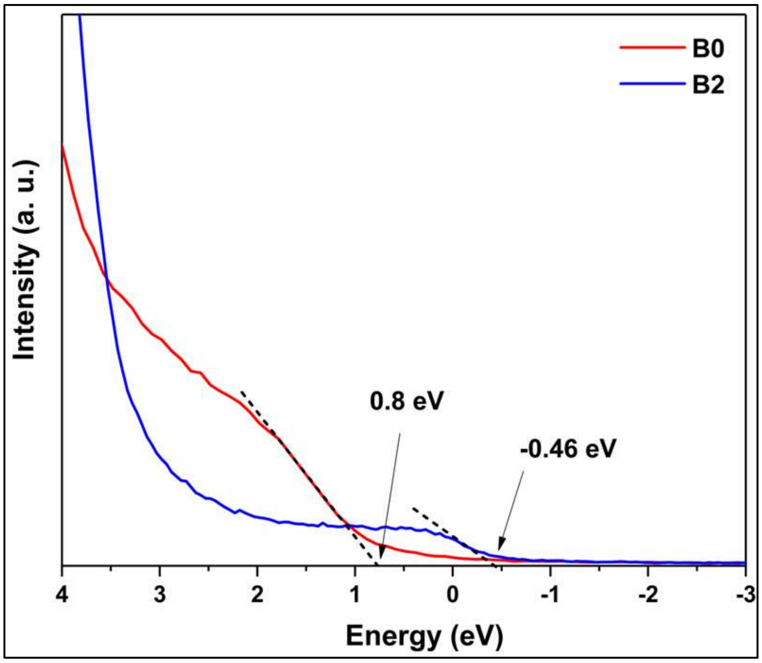

Figure 5.11 Valence band XPS spectrum of B0 and B2 samples.

Table 5.2 The position of VB and CB for the undoped and doped samples.

Samples	VB (eV)	CB (eV)
B0	0.80	-0.73
B1	-0.48	-2.18
B2	-0.46	-2.35

5.3.6 DFT calculation results

As mentioned earlier, the results of DFT calculations on different sulfur-doped models motivated the experimental investigations. The first calculations were on C0, CP1, and CP2 models. Table 5.3 describes the results of these calculations. The formation energy of a sulfur atom substituting oxygen (CP1) was lower than that found for CP2, indicating the former is favored thermodynamically.

Table 5.3 The formation energies and bandgap values of all the models attempted from DFT analysis.

Model	Formation energy (eV)	Bandgap (eV)
C0	-	0.00
CP1	0.71	0.06
CP2	1.97	0.0
C1	0.75	0.480
C2	0.63	0.54
C3	1.54	0.08
C4	1.81	0.518

It is crucial to note that the GGA-PBE functional used in the present investigation grossly underestimates the bandgap and gives a zero bandgap result for the pure Ag_2O model (De et al., 2020; Morales-García et al., 2017a). Sulfur substitution of oxygen (CP1) increased this bandgap (0.06 eV), qualitatively indicating that S-doping would increase the Ag_2O bandgap.

The next set of calculations attempted to elucidate the effect of oxygen vacancy on sulfur doping (or vice versa). Thus, S-doped OV-Ag_2O models (C2 and C3) are compared with the undoped OV-Ag_2O (C1) model. Table 5.3 summarizes the results of the DFT calculations on these systems. The calculated formation energy of the C2 and C3 models are 0.63 and 1.54 eV, respectively. Thus, substitutional doping (C2) is favored. The existence of sulfur in +4 or +6 oxidation states (from XPS) could be due to the formation of small Ag_2SO_3 and Ag_2SO_4 clusters. XRD would not detect these due to a lack of long-range order.

The substitutionally doped system (C2) also shows a larger bandgap (0.536 eV) than C1 (0.48 eV). Figure 5.12 gives the DFT calculated band structures of the C1 and C2 models, showing the bandgap. But, substitutional or interstitial S-doping causes lattice expansion in contrast to experimental (XRD) observation. Since S-doping also increases OVs, therefore DFT calculations were also conducted on another model with two only OVs (no S-doping). We denote this model by C4. Enhanced OVs contract the Ag_2O lattice (see Table 5.4). Furthermore, it also increases the bandgap (see Table 5.3).

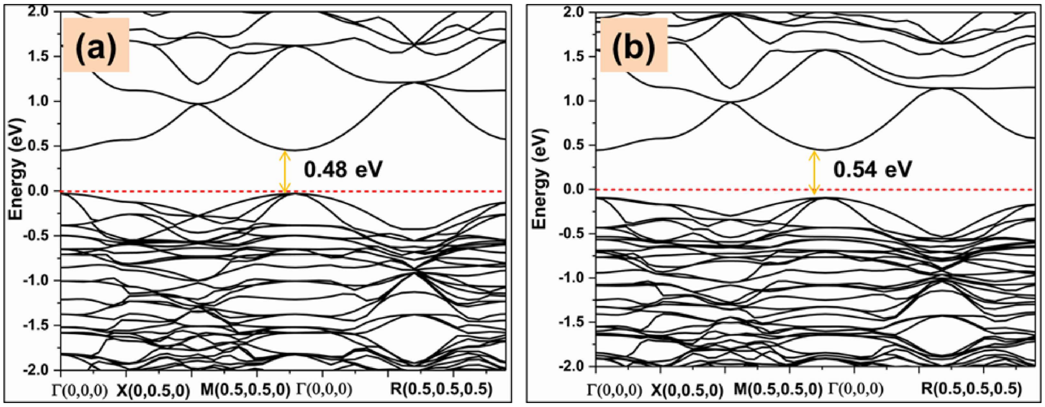

Figure 5.12 Band structure of (a) OV Ag_2O (C1 model), (b) OV Ag_2O with substitutional S doping (C2 model).

Table 5.4 Change of the lattice parameters on the increment of OV in Ag_2O lattice.

Lattice parameters	Without OV	1OV (C1)	2OV (C4)
A	9.63	9.53	9.46
B	9.63	9.53	9.45
C	9.63	9.53	9.46
α	90	90	90
β	90	90	90
γ	90	90	90
Volume	894.11	866.38	844.94

Figure 5.13 compares the TDOS of OV Ag_2O with the S-doped Ag_2O. The inset figure shows that the doped system states near the Fermi region shifted to the higher energy region. Note that the Fermi level is set at zero energy on the x-axis.

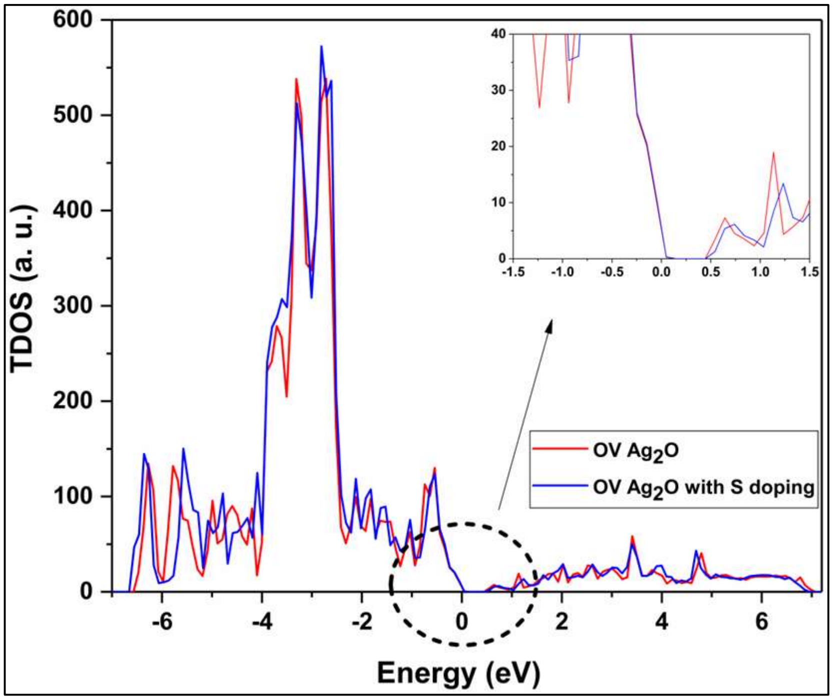

Figure 5.13 Comparison of TDOS of OV Ag_2O (C1 model) and S doped Ag_2O system (C2 model).

Given the lowest formation energy of C2, Figure 5.14 displays the total density of states (TDOS) and partial density of states (PDOS) of the respective atomic orbitals of the C2 model system. The VB and CB refer to the diagram's negative and positive energy regions. The O 2p and Ag 4d orbitals mainly contribute to the VB electron density.

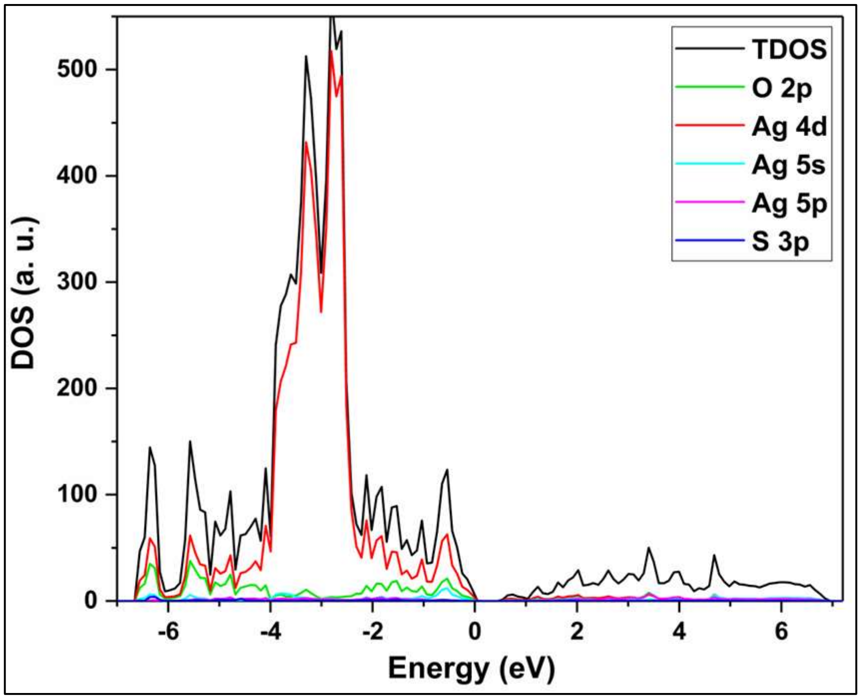

Figure 5.14 The TDOS and PDOS for OV Ag$_2$O with substitutional S doping system (C2 model).

On the other hand, the CB electron densities are primarily due to the Ag 5s and Ag 5p orbital. On S-doping, there is a considerable amount of hybridization between the atomic orbitals of Ag$_2$O (O 2p, Ag 4d, Ag 5s, Ag 5p) and dopant's atomic orbitals (S 3s, S 3p, and S 3d). As shown in Figure 5.15, the PDOS of S 3p is higher than those of S 3s and S 3d states and seems to be the main contributor to the electronic structure changes in S-doped Ag$_2$O.

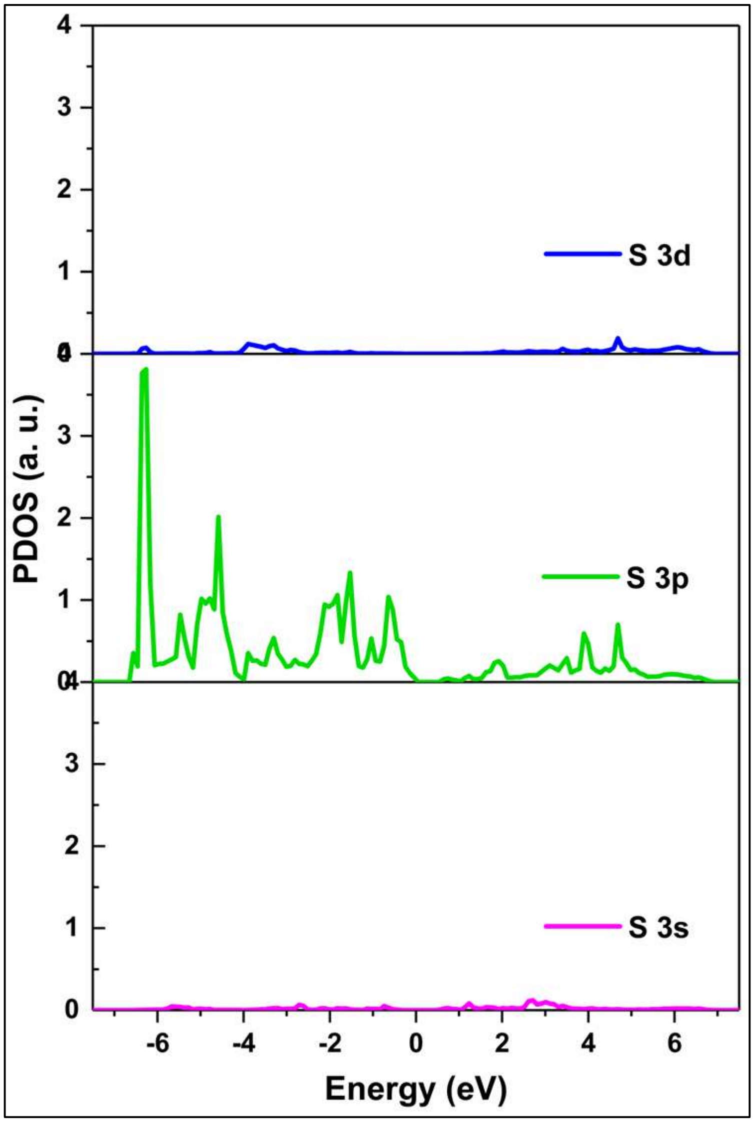

Figure 5.15 Comparison of PDOS of the dopant's atomic orbitals.

5.3.7 Photocatalytic properties

The visible photocatalytic activities of the as-prepared nanomaterials are tested for RhB degradation. Figure 5.16a shows the photocatalytic activities of the synthesized materials. RhB degrades at a higher rate on B1 and B2 than B0. But B2 exhibits the best RhB degradation activity.

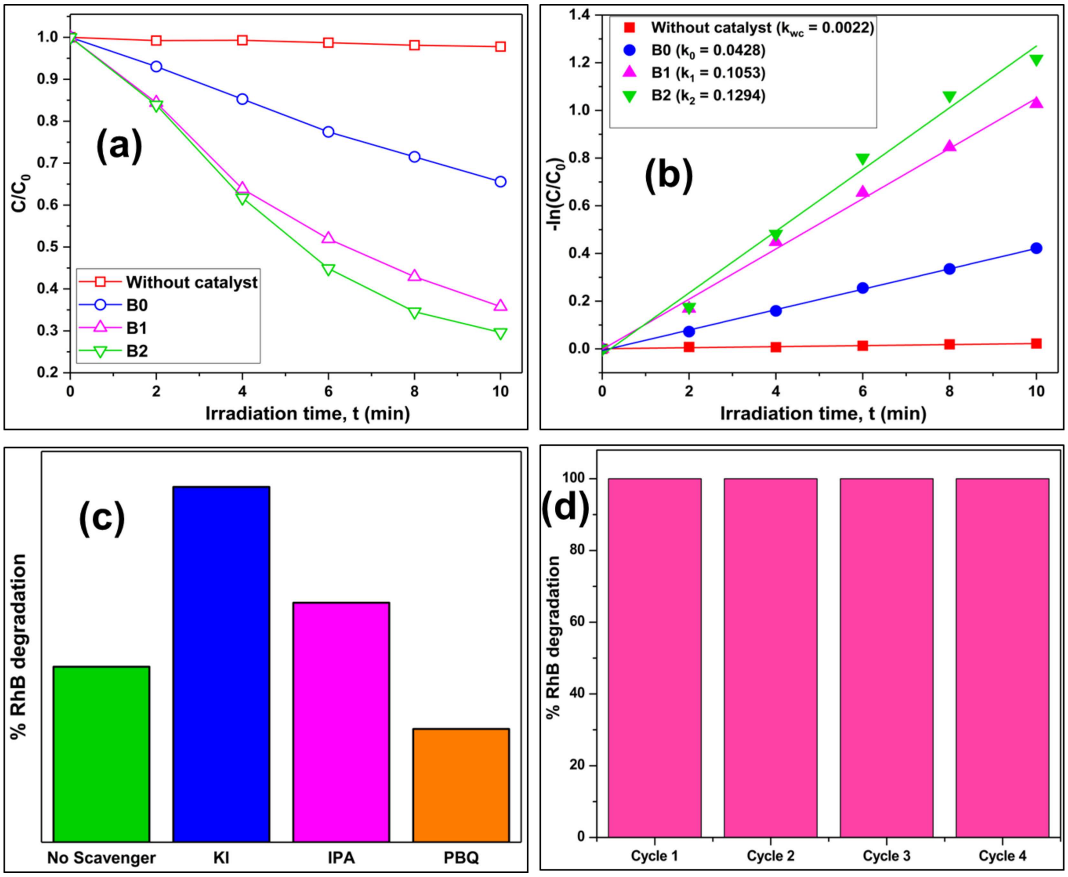

Figure 5.16 (a) Plots of RhB degradation with irradiation time, (b) kinetics plots – ln(C/C_0) vs. t over different photocatalysts, (c) results of scavenging experiments with on the B2 photocatalyst catalyst, and (d) recyclability tests of the B2 photocatalyst.

Figure 5.17(a) and (b) display the time variation of UV-visible absorption spectra of an aqueous solution of RhB over B0 and B2 photocatalysts. The B0 catalyst gives complete RhB degradation in 185 minutes. But RhB degradation over the B2 photocatalyst takes 35 minutes only.

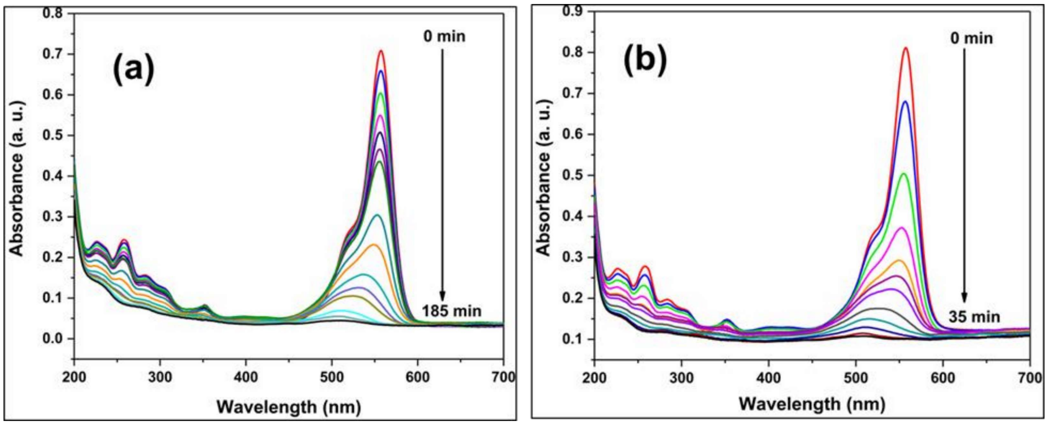

Figure 5.17 UV-Vis absorbance plot of RhB degradation on (a) B0 and (b) B2 photocatalysts.

There is no such degradation in the absence of a photocatalyst. RhB degradation over these photocatalysts follows pseudo-first-order kinetics (Eq. 5.4).

$$-\ln(C/C_0) = k_{app}t \qquad (5.4)$$

Here, C_0 is the initial concentration of the RhB aqueous solution, C is the concentration of the same after time t, and k_{app} is the apparent rate constant calculated from the slope of the linear fit to these plots. The kinetics plot is given in Figure 5.16b. The apparent rate constants were 0.0428, 0.1053, and 0.1294 min^{-1} for B0, B1, and B2 photocatalysts. The B2 photocatalyst shows the best catalytic activity on RhB degradation. Table 5.5 tabulates the turnover frequency (TOF) and apparent rate constant values for investigated photocatalysts.

The scavenging experiments were also performed to evaluate the reactive species during photocatalysis over the B2 sample (Figure 5.16c). Separate photocatalysis experiments were conducted with potassium iodide (KI), isopropyl alcohol (IPA), and p-benzoquinone (PBQ) for scavenging holes (h^+), hydroxyl radicals ($^{\cdot}OH$), and superoxide radicals ($O_2^{-\cdot}$), respectively. The addition of KI and IPA increased the RhB degradation rate compared to without any scavenger. In contrast, the addition of PBQ significantly reduces the RhB degradation rate. Therefore, the $O_2^{-\cdot}$ is the main active species during the RhB photodegradation. Figure 5.16d shows the result of the reusability experiment of the B2 photocatalyst. The photocatalyst exhibits very good recyclability up to four cycles.

Table 5.5 Turn over frequency (TOF) and rate constant of B0, B1, and B2 catalysts for the photo-degradation of RhB.

Catalysts	TOF (mole $g^{-1}min^{-1}$)	Rate constant (k_{app}) (min^{-1})
B0	4.79×10^{-6}	0.0428
B1	9.75×10^{-6}	0.1053
B2	1.18×10^{-5}	0.1294

5.3.8 Plausible photocatalytic mechanism

Figure 5.18 gives a schematic presentation of RhB photodegradation on the B2 photocatalyst. Visible light irradiation excited the electrons (e^-) on the VB to the CB. Oxygen vacancies and S-doping defects trapped the photo-excited species to reduce recombination probabilities. Further, it is well known that a small amount of Ag with Ag_2O helps to enhance the photocatalytic performance, increasing charge separation in the material. Metallic Ag can exhibit surface plasmon resonance (SPR) during light irradiation to enhance the photo efficiency and the charge carrier separation (Xuefei Wang et al., 2011; H. Xu et al., 2018). Light irradiation also led to photo-excitation of the RhB dye since its HOMO-LUMO gap is in the visible range. The photo-excited electrons were transferred from the LUMO of the dye to quench the holes on the photocatalyst VB. At the same time, the highly negative CB position led to superoxide formation, which in turn degraded RhB. But, photo-excited holes are quenched better by KI and IPA, increasing the photocatalytic kinetics compared to the situation with no scavenger molecule. The RhB molecule interaction with the photocatalyst surface seems weaker than that with KI and IPA.

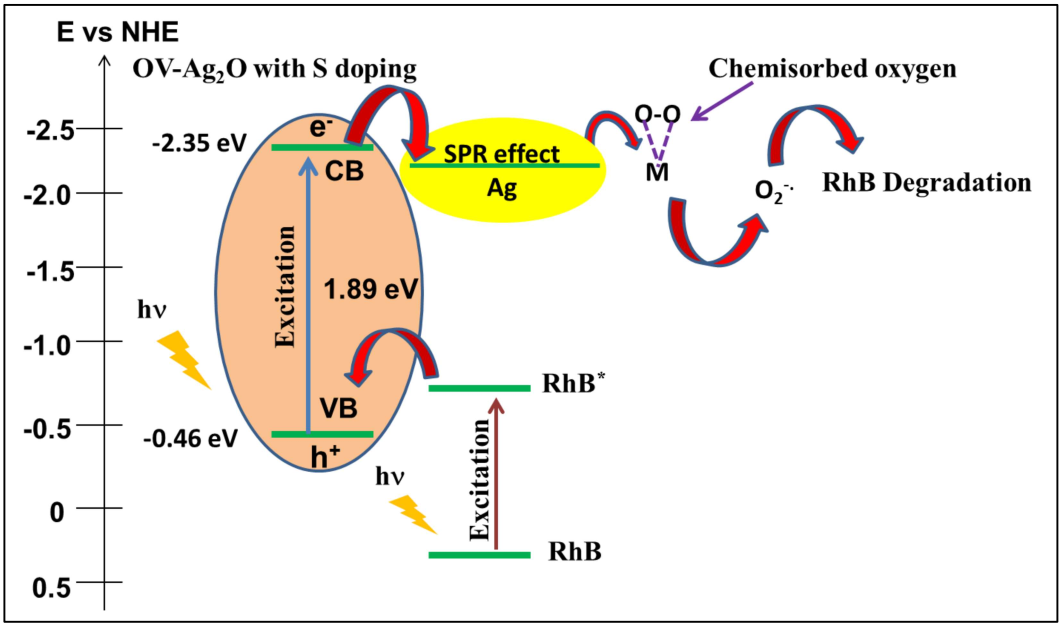

Figure 5.18 Possible RhB degradation photocatalytic mechanism.

S doping causes a shift of CB from -0.73 (B0) to -2.35 eV (B2). It also increases the OV proportion compared to the pure one. Further, these defects can also increase the charge separation in the doped systems. Therefore, higher CB potential and OVs in the doped Ag_2O facilities faster superoxide radicals formation, mainly responsible for the enhanced degradation efficiency in the doped samples.

5.4 Conclusions

Motivated by initial DFT predictions, sulfur-doped Ag_2O nanoparticles were prepared by a hydrothermal precipitation protocol. Sulfur doping could be achieved only up to 1.25%. Doping beyond this percentage led to the formation of multiple compound phases (Ag_2SO_3, Ag_2SO_4, etc.). Sulfur-doping up to 1.25% increased the bandgap substantially to 1.89 eV. DFT calculations predicted that substituting oxygen with sulfur could widen the Ag_2O bandgap and stabilize oxygen vacancies.

Furthermore, increased oxygen vacancies contracted the doped-Ag_2O lattice. XPS analysis also showed that sulfur-doping increases oxygen vacancies. Photoluminescence investigations showed that recombination probability decreased with doping. The photocatalytic activity of the Ag_2O nanoparticles towards rhodamine B degradation increased with sulfur doping. The substantial change in the electronic structure of Ag_2O nanoparticles due to oxygen vacancy and sulfur doping implies that these are virtually new photocatalysts.

CHAPTER 6: Cd doped $Ag_2O/BiVO_4$ photocatalysts

6.1 Introduction

Doping a semiconductor photocatalyst can change its electronic structure and induce charge separation, resulting in delayed recombination (Gong et al., 2020; Haiping Li et al., 2020; Jianbin Liu et al., 2021; Murali et al., 2021; Negishi et al., 2012). The bandgap, valence band (VB), or conduction band (CB) positions are also affected. For instance, Natu et al. reported cobalt doping shifts the VB position of NiO (Natu et al., 2012). In another study, Wang et al. executed a detailed DFT investigation of the effect of oxygen doping on the Ta_3N_5 photocatalyst. The oxygen doping changed the bandgap and band edges of the Ta_3N_5 photocatalyst (Jiajia Wang et al., 2014). Doping also affects the adsorption properties of the parent photocatalyst (Andjelkovic et al., 2014; Jie Chen et al., 2020; Panneri et al., 2017). Hence, doping affects the photocatalyst's bandgap, band positions, and adsorption behavior. Therefore, doping could effectively produce a new photocatalyst with different photocatalytic properties.

More intensive use of medium and small bandgap (corresponding to the visible range) semiconductors is necessary for fabricating photocatalysts that can optimally utilize the UV-visible part of the solar spectrum. For instance, photostability or photo corrosion of (small bandgap) Ag_2O has hampered its photocatalytic applications. Doping Ag_2O or its composite formation with another photocatalyst could significantly reduce the problem while improving excited species charge separation (H. Xu et al., 2018). A recent DFT study on Zn-doping in Ag_2O revealed that such inclusion could shift the VB of the Ag_2O to a higher positive value (De et al., 2020). In another report, Sr doping also resulted in Ag_2O bandgap widening (Kiani et al., 2019). Recently, De et al. showed that Ni doping could shift the VB and CB edge of the Ag_2O photocatalyst to a more positive and less negative value. The higher valence Ni^{2+} substituted Ag^{+} to give the host system excess electrons (De & Sinha, 2022). Thus, the strategy of doping Ag_2O can provide a photocatalyst with a tunable band structure with distinct properties.

Doping and composite formation with another semiconductor can change a photocatalyst's reduction and oxidation driving forces along with the excited species charge separation. Hence, a doped Ag_2O material as part of a composite should give an improved photocatalyst. There have been a few investigations on Ag_2O-based composites (or photocatalytic heterostructures). For instance, there are reports on the fabrication and evaluation of $ZnO/Ag/Ag_2O$, Ag_2O/TiO_2, $BiVO_4/Ag/Ag_2O$, Ag_2O/Bi_2O_3, etc., photocatalysts (L. Chen et al., 2019; Sahu & Das, 2022; Ullah et al., 2020; L. Zhu et al., 2012). But to date, we have not encountered any doped Ag_2O-based heterojunction or composite photocatalyst.

In the present research, we investigated the photocatalytic properties of Cd-doped Ag_2O, and its composite with $BiVO_4$. Note that neither synthesis nor the photocatalytic properties of Cd doped-Ag_2O have been reported in published literature. The first part of this research evaluated whether Cd substitutes Ag or occupies an interstitial position through density functional theory (DFT) calculation of the formation energies of the two models. Simultaneously, Cd-doped Ag_2O nanoparticles were prepared by a hydrothermal precipitation protocol. X-ray diffraction (XRD) results agreed with the DFT defect formation energy prediction. X-ray photoelectron spectroscopy (XPS) investigated the chemical species and the VB position in the Cd-doped Ag_2O nanoparticles. Separately, a well-established hydrothermal protocol was employed to prepare monoclinic $BiVO_4$. In the next step, another hydrothermal strategy joined these nanoparticles to Cd-doped Ag_2O nanostructures. The prepared composite particles were characterized using different techniques. The composite nanoparticles were evaluated for photocatalytic ciprofloxacin (CIP) degradation activity under visible light irradiation. CIP is frequently administered to human patients and excreted in a partially metabolized state. The latter makes the target microorganisms in the environment resistant to the antibiotic in question. Photocatalytic activities with different active species scavenger molecules probed the underlying photocatalysis mechanism. Parallelly, DFT calculations ascertained the adsorption energies of oxygen and H_2O on the Cd-doped Ag_2O and $BiVO_4$ surfaces. The information collated was used to propose a plausible photocatalysis mechanism.

6.2 Experimental

6.2.1 Sample preparation

6.2.1.1 Synthesis of Cd doped Ag_2O

A hydrothermal protocol was followed to prepare Cd-doped Ag_2O. Two millimoles (mmol) of $AgNO_3$ (Merck) were fully dissolved in 50 ml deionized double distilled water (DDDW) with continuous stirring on a magnetic stirrer. Then, 0.2M NaOH was added drop-by-drop into the stirring solution until the solution pH reached 11. A brown-colored precipitate was formed during the addition. The stirring was continued for 15 minutes. Next, the desired amount of $Cd(NO_3)_2.4H_2O$ (Merck) aqueous solution was added to the previously obtained mixture. Stirring was continued for another 15 minutes, and then the reaction mixture was transferred to a 100 ml stainless steel autoclave. The latter was put in a hot air oven at 180°C for 24 hours. We prepared three different compositions of Cd-doped Ag_2O samples abbreviated as D1, D2, and D3. These contained 0.3, 0.62, and 1.25-mole percent of $Cd(NO_3)_2.4H_2O$. In addition, the pure Ag_2O (denoted as D0) was also synthesized by the same hydrothermal protocol but without $Cd(NO_3)_2.4H_2O$ addition.

6.2.1.2 Synthesis of $BiVO_4$

Aqueous solutions of $Bi(NO_3)_3.5H_2O$ (Merck) and NH_4VO_3 (HIMEDIA) were prepared in two separate beakers. In one beaker (A), 20 ml of 4M HNO_3 was directly mixed with 4 mmol of $Bi(NO_3)_3.5H_2O$ salt with continuous stirring until the formation of a clear solution. In another beaker (B), 4 mmol of NH_4VO_3 was dissolved in 20 ml of 4M NaOH by continuous stirring. Stirring was continued in both beakers for 30 minutes. The solution in beaker B was added drop-by-drop into beaker A in the next step. The formation of a yellow-colored precipitate was observed. Next, the reaction mixture pH was adjusted to 7 by adding an appropriate amount of NaOH. This reaction mixture was stirred for another 25 minutes and then transferred to a 100 ml autoclave reactor for hydrothermal treatment at 180°C. After 20 hours of hydrothermal treatment, the reaction mixture was allowed to cool. The precipitate formed was separated and washed with DDDW several times until the water used in washing had neutral pH. Finally, the as-prepared precipitate was rewashed with ethanol and dried at $60^{\circ}C$ under a hot air oven to get the $BiVO_4$ nanoparticles (abbreviated by 'V0' in the rest of the Chapter).

6.2.1.3 Synthesis of $BiVO_4$/Cd-doped Ag_2O

The D1 sample (of Cd-doped Ag_2O) was mixed with 5, 10, and 20 weight% of $BiVO_4$ nanoparticles in 60 ml DDDW to prepare three separate systems abbreviated as D1/5V, D1/10V, and D1/20V. The three mixtures were stirred for 4 hours to induce interaction between Cd-doped Ag_2O and $BiVO_4$ nanoparticles. These mixtures were transferred to 100 ml autoclave reactors and subjected to hydrothermal treatment for twelve hours at 120°C. Afterward, the prepared material was separated from the supernatant and dried at 50°C overnight in a hot air oven.

6.2.2 Computational methods

The plane-wave density functional theory (DFT) calculations were done on the Medea VASP (Vienna ab-initio simulation package) software. The calculations used generalized gradient approximation Perdew-Burke-Ernzerhoff (GGA-PBE) exchange-correlation functional and the projected augmented wave (PAW) pseudopotentials. A $2 \times 2 \times 2$ supercell was built from the Ag_2O unit cell (ICDS Card No. 4318188) and was optimized using $2 \times 2 \times 2$ k-points and 520 eV energy cut-off. The optimized supercell is labeled as P0 in the rest of the chapter. The doped Cd atom could substitute an Ag atom or occupy an interstitial position in the Ag_2O lattice. Thus, in one model (denoted as P1), one Cd substituted an Ag atom in the Ag_2O supercell. In another model (denoted as P2), a Cd atom was placed in an interstitial position of the Ag_2O lattice. These two models were optimized with the same calculation parameters as mentioned above. After that, the defect formation energies of the two doped systems were calculated using the following equations.

$$E_f(Sub) = E_{defect}(P1) - [E_{perfect}(P0) - \mu_{Ag} + \mu_{Cd}] \qquad (6.1)$$

$$E_f(Inter) = E_{defect}(P2) - [E_{perfect}(P0) + \mu_{Cd}] \qquad (6.2)$$

Here, $E_f(Sub)$ and $E_f(Inter)$ are the defect formation energy of the substituted and interstitially doped systems. $E_{defect}(P1)$, $E_{defect}(P2)$, and $E_{perfect}(P0)$ are the energies of the P1, P2, and P0 models, respectively. The energy per atom in Ag and Cd metallic unit cells gives the chemical potentials of the Ag and Cd (μ_{Ag} and μ_{Cd}). The adsorption energies (E_{abs}) of H_2O and O_2 on Cd-doped Ag_2O (200) and $BiVO_4$ (112) surfaces were evaluated by slab model calculations using equation 6.3. First, the Ag_2O

supercell was cleaved to obtain its (200) surface, and then an Ag atom was replaced with a Cd atom to construct the Cd-doped Ag_2O (200) slab. Similarly, the $BiVO_4$ supercell was cleaved to get its (112) surface. A four-layer slab with a vacuum of 10 Å was considered for both models. The slab dimensions for Cd doped Ag_2O (200) and $BiVO_4$ (112) surfaces were $6.69 \times 6.69 \times 28.92$ and $6.93 \times 7.32 \times 96.99$, respectively.

$$E_{abs} = E_{slab+adsorbate} - (E_{slab} + E_{adsorbate}) \tag{6.3}$$

Here, $E_{slab+adsorbate}$ is the energy of the slab with the adsorbate molecule. E_{slab} and $E_{adsorbate}$ are the energies of the individual free slab and the free adsorbate molecule.

6.2.3 Photocatalytic experiment details

A 2 ml aqueous solution of CIP (10 ppm) at pH~3 and $100\mu l$ of the re-dispersed photocatalyst aqueous suspension (1 mg/ml) were mixed properly in a 4 ml quartz cuvette. The mixture was allowed to stand in a dark environment for 35 minutes under continuous stirring until adsorption-desorption equilibrium. Then the cuvette was kept under visible light irradiation (14W Philips LED bulb with an intensity of 720 W/m^2). The absorbance of the reaction mixture was recorded at regular time intervals to monitor the photocatalytic activities of the synthesized materials. Turnover frequencies (TOF) were also calculated.

6.3 Results and discussion

6.3.1 Structural properties

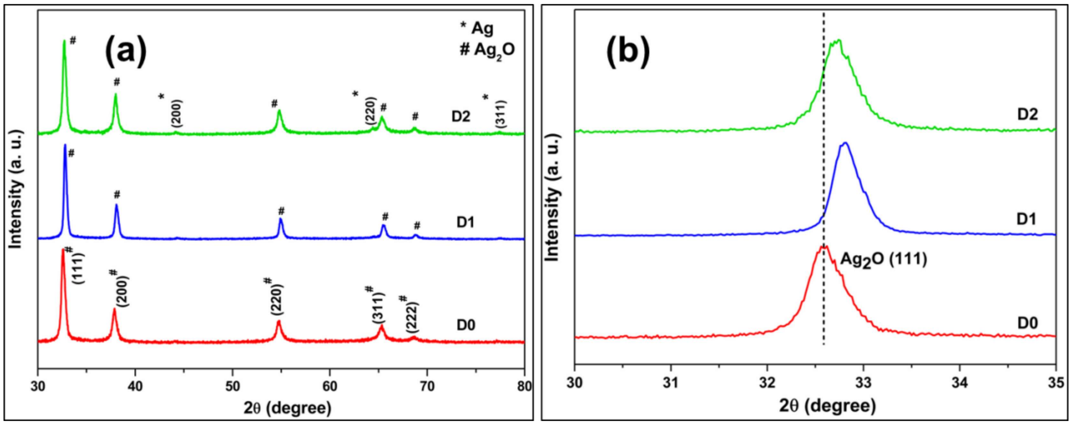

Figure 6.1 (a) The powder XRD patterns of undoped (D0) and doped samples (D1 and D2) (b) the zoomed-in Ag_2O (111) peak part.

Figure 6.1(a) displays the powder XRD pattern of the undoped (D0) and different Cd-doped Ag_2O nanoparticle samples (D1 and D2). All the peaks in the XRD plots of D0 and D1 match the standard FCC Ag_2O (JCPDS Card No. 75-1532) pattern. Other phases are not present in the D1 sample. Nonetheless, the XRD of D2, in addition to the FCC Ag_2O peaks, also clearly displays three small peaks of the FCC Ag phase. The formation of reduced Ag is due to the excess electrons supplied by the dopant when added beyond a specific limit. Furthermore, the XRD pattern of sample D3 displayed peaks of phases other than FCC Ag_2O and Ag (Figure 6.2) when the dopant level increased to 1.25 mol%. CdO_2 peaks in Figure 6.2 are matched with the standard JCPDS database Card No.391221, which is cubic primitive (space group: $Pa\overline{3}$) crystal structure of CdO_2.

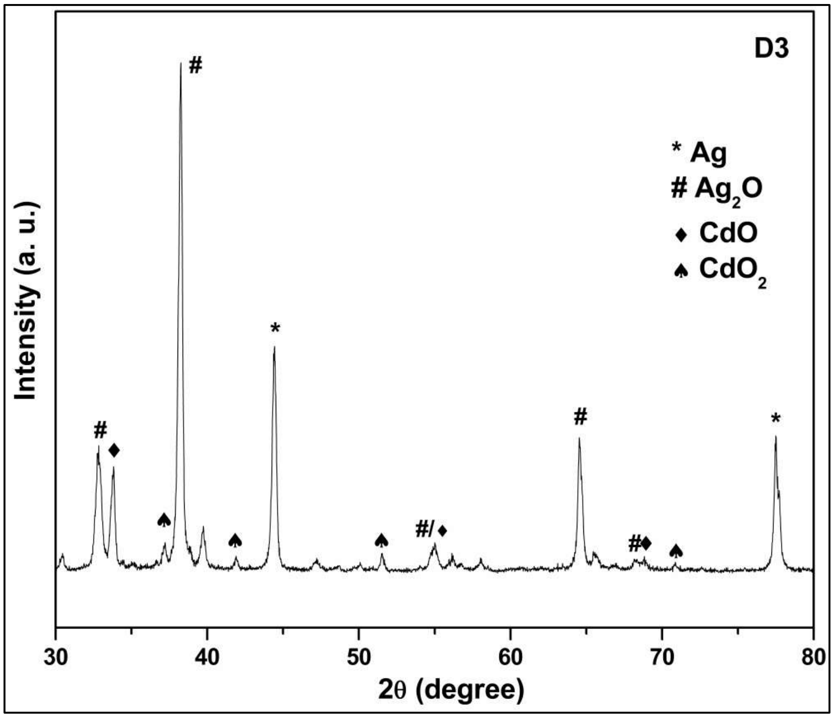

Figure 6.2 Powder XRD pattern of D3 sample.

Figure 6.1(b) compares the (111) plane peak positions of D0, D1, and D2 samples. The (111) peak position shifts towards higher 2θ regions in doped samples, indicating lattice contraction. Nevertheless, the peak shift is not uniform. The smallest dopant percentage sample (D1) gave the maximum peak shift. The Cd^{2+} and Ag^{+} have effective ionic radii of 95 and 115 pm. As mentioned earlier, the dopant (Cd^{2+}) has two choices: it can substitute one Ag or go into the interstitial sites in the Ag_2O lattice. Lattice contraction is only viable if smaller Cd substitutes Ag in the Ag_2O lattice. The D1 dopant sample was selected to prepare composite materials with $BiVO_4$ since it showed substitutional doping of Cd in the Ag_2O lattice without FCC Ag formation.

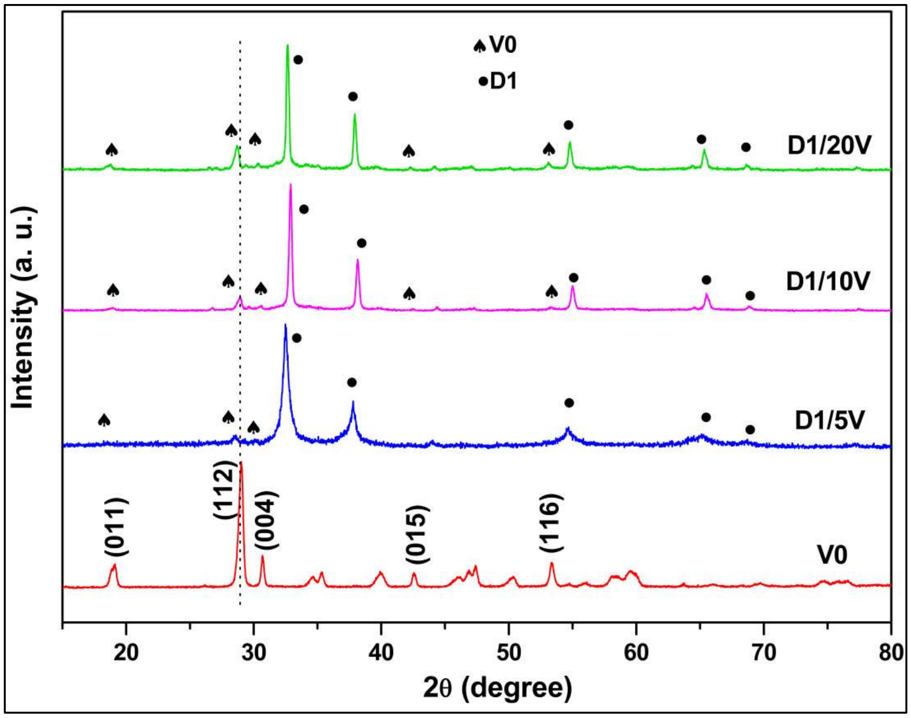

Figure 6.3 Comparison of powder XRD pattern of $BiVO_4$ nanoparticles and composite samples (D1/5V, D1/10V, D1/20V).

Figure 6.3 compares the powder XRD patterns of the composite materials with those of $BiVO_4$ (V0) and D1 samples. The XRD pattern of sample V0 matches the standard body-centered monoclinic (JCPDS Card No. 831699) phase of $BiVO_4$. The major peaks in the XRD at 18.9°, 29°, 30.7°, 42.5°, and 53.4° are indexed to the (011), (112), (004), (015), and (116) planes of the body-centered monoclinic $BiVO_4$. The XRD of all composite samples showed the presence of both Ag_2O and $BiVO_4$ phases, indicating nanocomposite formation (Jatav et al., 2021). Hereafter, the investigation concentrates on D1/10V sample characterization because of its enhanced photocatalytic activity (compared to D1/5V and D1/20V composites) towards CIP. Figure 6.4(a) and (b) exhibit the TEM and high-resolution TEM (HRTEM) images of the D1/10V composites. The high-resolution image of the encircled region (in Figure 6.4a) shows two types of fringes adjacent to each other. These fringe spacings match the d-spacing of $BiVO_4$ (011) and Ag_2O (111) planes, confirming D1/10V composite formation.

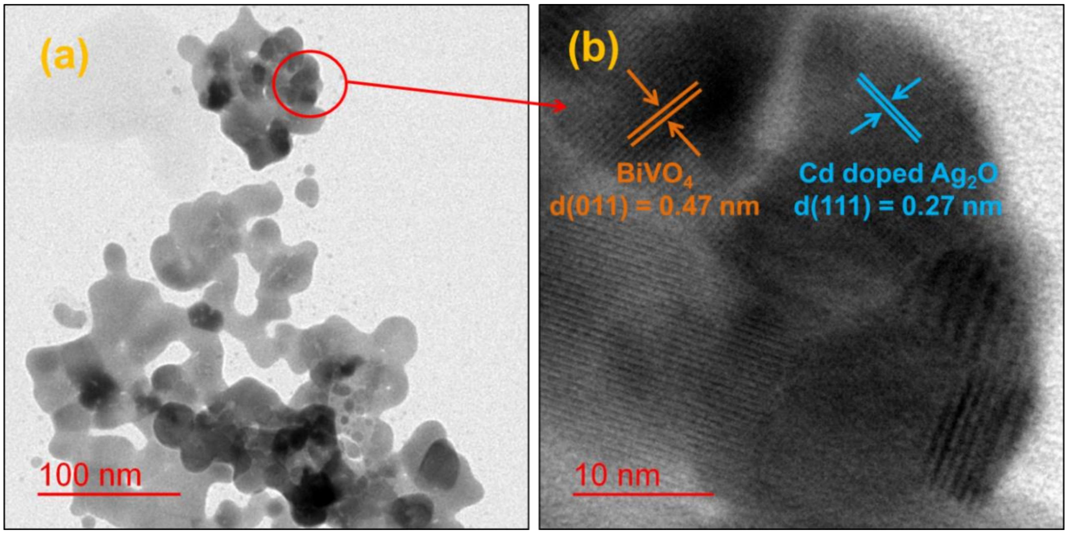

Figure 6.4 (a) TEM and (b) HRTEM images of the D1/10V sample.

6.3.2 XPS analysis

XPS investigation gives information about elements and their oxidation states in a material. Figure 6.5 shows the Ag 3d high-resolution XPS plots of samples D0 and D1. The Ag $3d_{3/2}$ and Ag $3d_{5/2}$ peaks at 374.28 and 368.26 eV for D0 shift to 373.75 and 367.73 eV for the D1 sample. The extra electrons injected into the system by the Cd dopant made D1 electron-rich, causing the shift of respective Ag 3d peaks to lower binding energies.

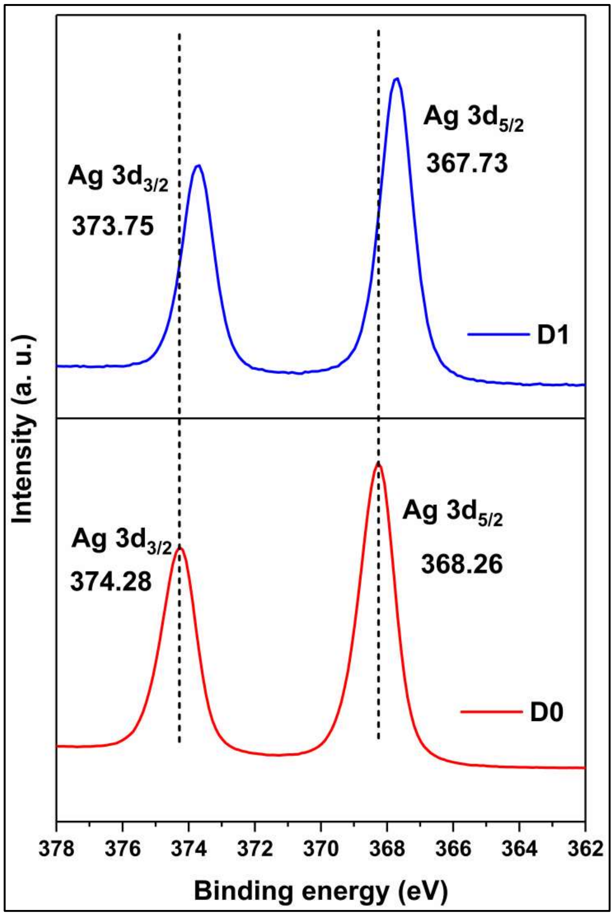

Figure 6.5 Comparison of high-resolution Ag3d spectra of D0 and D1 samples.

The XPS survey spectrum of the D1/10V composite shows the presence of Ag, Bi, V, and O elements in the composite (see Figure 6.6).

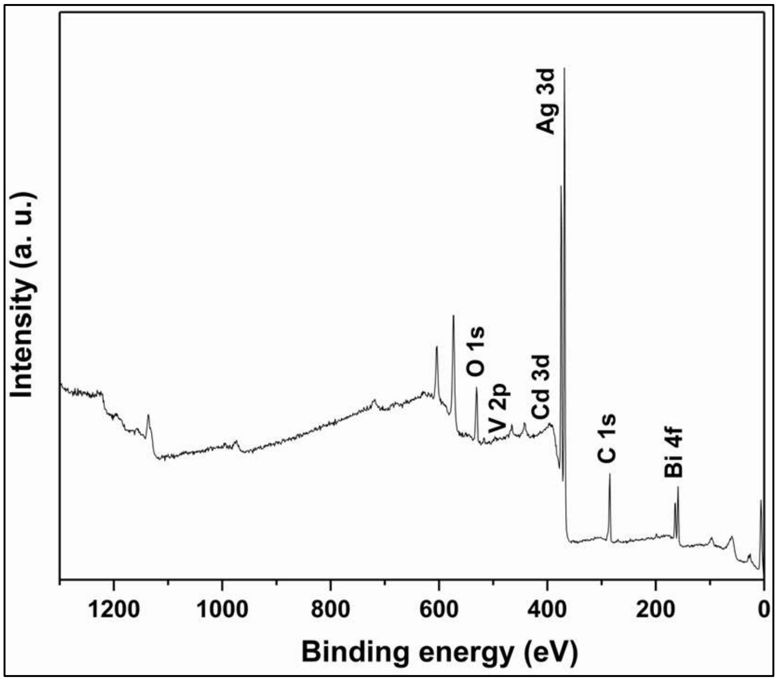

Figure 6.6 XPS survey spectrum of D1/10V sample.

Figure 6.7(a) compares the Ag 3d region high-resolution XPS plots of D1 and D1/10V samples. The Ag $3d_{5/2}$ and Ag $3d_{3/2}$ peaks at 367.71 and 373.74 eV for D1 shifted to higher values (Ag $3d_{5/2}$ at 368.15 and Ag $3d_{3/2}$ at 374.18 eV) in the D1/10V composite spectrum. Simultaneously, the Bi 4f spectrum with two peaks corresponding to Bi $4f_{7/2}$ at 158.96 and Bi $4f_{5/2}$ at 164.26 eV shifted to lower binding energy in the composite sample (Bi $4f_{7/2}$ at 158.70 and Bi $4f_{5/2}$ at 164.01 eV) (see Figure 6.7b). The shift to higher binding energies of Ag 3d peaks and lower binding energies of the Bi 4f peaks implies electron transfer from the Cd doped Ag_2O (D1) to $BiVO_4$ (V0). Figure 6.7(c) and (d) display the valence band XPS plots of D1 and D1/10V samples. The VB edge of the D1 sample is at 2.67eV, and $BiVO_4$ (V0) is at 1.34 eV. Note that the VB position of the D0 (undoped Ag_2O) sample is at 0.8 eV. Hence, Cd-doping of Ag_2O causes a severe shift in the VB position of the sample. A Z-scheme electron transfer mechanism seems to operate in this composite since the component with more negative